Geophys. J. Int. (2002) **148,** 402–425

Numerical simulation of first-order backscattered *P* and *S* waves for time-lapse seismic imaging in heterogeneous reservoirs

P. C. Leary*

Geospace Engineering Resources International, Stafford, TX, USA

Accepted 2001 August 7. Received 2001 July 31; in original form 2001 February 5

SUMMARY

First-order elastic wave scattering theory, validated in general features by deep-borehole seismic coda wave observations, is used to numerically simulate time-lapse borehole seismic data aimed at monitoring oil–water substitution in heterogeneous hydrocarbon reservoirs. A first-order perturbation solution of the vector wave equation leads to *P*–*P* and *S*–*S* backscattered displacement vector motion expressed as the angular summation of the second radial derivative of *P*- and *S*-wave velocity and density fluctuations α'/α, β'/β, ρ'/ρ over expanding spherical wave fronts of radii $\xi = \alpha t/2$ and $\xi = \beta t/2$. *P*- and *S*-wave velocity and density spatial heterogeneity is modelled as long-range correlated random fluctuations consistent with the power-law-scaling character of crustal rock physical properties measured by borehole logs. The spectra of model scattering displacement seismograms for a power-law-scaling volumetric noise distribution duplicate the frequency enrichment observed in the spectra of broadband earthquake coda waves recorded in a deep well. Modelling of time-lapse scattering in power-law-scaling permeability structures suggests that a stable borehole seismic source can locate oil–water substitution in reservoir volumes tens of metres on a side at distances of up to a few hundred metres from an observation well using currently available borehole seismic technology. Time-lapse tracking of oil–water substitution and the monitoring of reservoir stress conditions can lead to spatially well-constrained reservoir models, despite large-scale, large-amplitude correlated random heterogeneity.

Key words: reservoirs, scattering, statistical methods, synthetic seismograms.

1 INTRODUCTION

This paper develops a numerical model of time-lapse borehole seismic backscatter imaging using a source and sensors operating in a single oilfield production well. The goal is to provide cost-effective images of progressive oil–water substitution volumes by using available borehole installations to map the large-scale drainage structure of heterogeneous hydrocarbon reservoirs.

1.1 Time-lapse hydrocarbon reservoir seismic monitoring

Hydrocarbon distribution and flow in heterogeneous rock depends variously on dynamic fluid diffusion parameters—flow rates, pressures, temperatures, relative permeabilities and saturation—and on quasi-static rock structure—porosity, pore-connectivity, large- and small-scale flow barriers, variable lithology and microcrack alignment. Experience indicates that the spatial variation of hydrocarbon distribution and flow is usually too complex to model reliably using stochastic methods constrained by small-scale well-core data (e.g. Francis & Pennington 2001). Since inaccurate reservoir models lead to inefficient and incomplete hydrocarbon recovery, the increased demand for more efficient and complete hydrocarbon recovery, particularly in offshore oilfields, fuels the need for better methods to determine the large-scale flow-heterogeneity structure of draining reservoirs (van Riel 2000; Oil & Gas Industry Task Force 2001; Francis & Pennington 2001).

A direct way to address the reservoir drainage heterogeneity problem is to observe the spatial position of changing reservoir fluids through time-lapse seismics (Sparkman 1998; Christie & Ebrom 2000; Jack 2001; Tura & Cambois 2001; Gutierrez, Dvorkin & Nur 2001). Time-lapse seismic monitoring of hydrocarbon production is well established in principle. Stable seismic sources and sensors take repeat 'snapshots' of a crustal reservoir containing gas, oil and/or water. As one fluid phase displaces another during fluid injection or extraction, part of the reservoir undergoes a change in elastic properties due to its changing pore fluid content. Provided the sources and sensors are sufficiently stable and ambient noise is sufficiently small, the significant changes in the 'snapshot' seismograms are due to the changes

* Now at: 28 Howard Place, Edinburgh, EH3 5JY, UK. E-mail: pcleary_mog@compuserve.com

in fluid properties within localized fluid substitution volumes. By comparing a time sequence of stably sourced and sensed seismograms, the reservoir drainage structure can be spatially mapped from progressive changes in the amplitude and/or phase of a few seismic backscatter wavelets.

Early demonstrations of the time-lapse seismic monitoring principle are presented in Sheriff (1992). Specific examples include surface seismic tracking of *in situ* combustion (Greaves & Fulp 1987), oil–water substitution (Dunlop *et al.* 1988), and steam-fronts in tar sands (Pullen *et al.* 1987; Matthews 1992). In addition, cross-well acoustic tomography has successfully surveyed enhanced recovery by heat-injection (Justice *et al.* 1989; Paulsson *et al.* 1994). Martin & Davis (1987) discuss shear wave polarization changes due to changes in aligned fractures during production; Talley *et al.* (1998) use time-lapse seismics to monitor a CO_2 flood for reservoir flow anisotropy and permeability structure. With time, more extensive surveys of large-scale production systems were essayed with repeat surface seismic surveys, highlighting the importance of the time-lapse images, but also the need for repeatable sources and stable sensors in acquiring useful time-lapse images (Christie & Ebrom 2000; Dumont *et al.* 2001). The case for permanently instrumented oilfields is discussed by Ebrom *et al.* (2000).

Current experience shows, however, that stable time-lapse surface seismic and/or acoustic tomographic infrastructure can be costly, and data acquisition and processing can be time-consuming (Oil & Gas Industry Task Force 2001). Costs may be particularly significant for offshore hydrocarbon reservoir monitoring requiring seafloor installations. A potentially efficient scheme for time-lapse reservoir monitoring is to exploit production wells in order to place seismic sources and sensors in closer proximity to reservoir fluid fronts. The required imaging infrastructure reduces to a sensor string placed outside the production tubing at reservoir depth, and a compact, benign and stable seismic source deployed periodically in the well at reservoir depth. Processing and interpreting the seismic backscatter 'reflection snapshots' is straightforward, speedy and low cost.

As with most time-lapse seismics, the essential issue is the source signal strength. The signal strength of time-lapse seismic backscatter images acquired with a source and a sensor string in a production well must be assessed before practical attempts can be made to implement the scheme. Signal strength must meet two criteria: (1) the absolute backscattering signal must exceed uncorrelated random background seismic noise in the sensor string; and (2) the relative time-lapse signal must exceed observational noise levels due to variations in seismic backscattered waves arising from a variable source wavelet.

An accurate assessment of the time-lapse backscattering signal strength requires folding the source and sensor performance data into suitable physical models of fluid-filled reservoir rock and the seismic scattering process. A data-driven reservoir heterogeneity model is discussed in Sections 1.2 to 1.4, and the appropriate first-order seismic backscattering formalism is derived in Sections 2.1 to 2.4 (see Appendix A for a full list of the notation used). Sections 3.1 and 3.2 calibrate the resulting model backscattering seismograms against deep-well observations of earthquake-generated scattering data. Recent borehole source performance data are used in Section 4 to illustrate the strength and stability of the time-lapse backscatter image signals available with current technology at small source–sensor offsets. Section 5 extends the backscattering imaging formalism to the wide source–sensor offsets deployed for multisource, multisensor static imaging data. The modelling results are summarized in Section 6.

1.2 Generic reservoir fracture heterogeneity

An accurate estimate of the seismic scattering in reservoir rock requires good physical control of elastic property spatial variation. Borehole logs provide a rich source of physically accurate data on the spatial variation of reservoir-rock physical properties (Leary 1991; Turcotte 1992; Al-Kindy 1999). A large number of logs and well-core sequences indicate that reservoirs, and crustal rock in general, are characterized by a generic stochastic spatial heterogeneity associated with fracture and fluid percolation (Leary 1997, 1998). In particular, Leary & Al-Kindy (2002) find from well-core porosity and permeability sequences of a producing North Sea oilfield that: (1) porosity and log (permeability) fluctuations are 80 per cent spatially cross-correlated in hydrocarbon-bearing sandstones; and (2) the well-core porosity and permeability fluctuations have the same power-law-scaling random spatial correlation as seen extensively in borehole logs. It follows that reservoir flow heterogeneity is physically intimately associated with the spatial heterogeneity recorded in hundreds of well logs.

Fig. 1 encapsulates the physical model for computing backscattering seismograms, and illustrates the importance of the time-lapse imaging of draining reservoirs. The left-hand column shows two examples of random spatial property fluctuations. The 2-D spatial distributions are slices from a single 3-D model spatial distribution controlled by well-log and well-core fluctuation statistics. That is, the two left-hand distributions of Fig. 1 are such that any borehole log drilled along the slice would produce spatial fluctuations that are statistically consistent with spatial fluctuations observed *in situ*.

The central and right-hand columns of Fig. 1 partition the left-hand column distributions by scale-length range to show the essential physical features of crustal rock stochastic fluctuation distributions: the significant stochastic spatial fluctuations are associated with large scale-lengths (centre column) rather than small scale-lengths (right-hand column).

The central column distributions extract from the left-hand column the spatial fluctuations that occur over large scale-lengths (Fourier spatial frequencies 1–8), while the right-hand column distributions show the small-scale-length fluctuations (Fourier spatial frequencies 9–128). The large-amplitude, large-scale stochastic spatial flow variability of the central column captures the spatial drainage fluctuation properties of the left-hand distributions, but the small-amplitude, small-scale spatial fluctuations of the right-hand columns carry no information about the large-scale spatial random structures that control the reservoir drainage pattern. Since individual well-core samples contain only small-scale spatial information about reservoir structure, it follows from Fig. 1 that the important large-scale heterogeneous reservoir structure cannot be reliably inferred from small-scale fluctuation data. The large-scale structures of the central column are, however, the essential drainage structures that a reservoir model should seek to incorporate. The Fig. 1 central column structures are, consequently, the target of high-resolution time-lapse borehole seismic imaging. The small-scale structures of the right-hand column provide seismic scattering background noise, whose contribution to the scattering seismograms also needs to be computed.

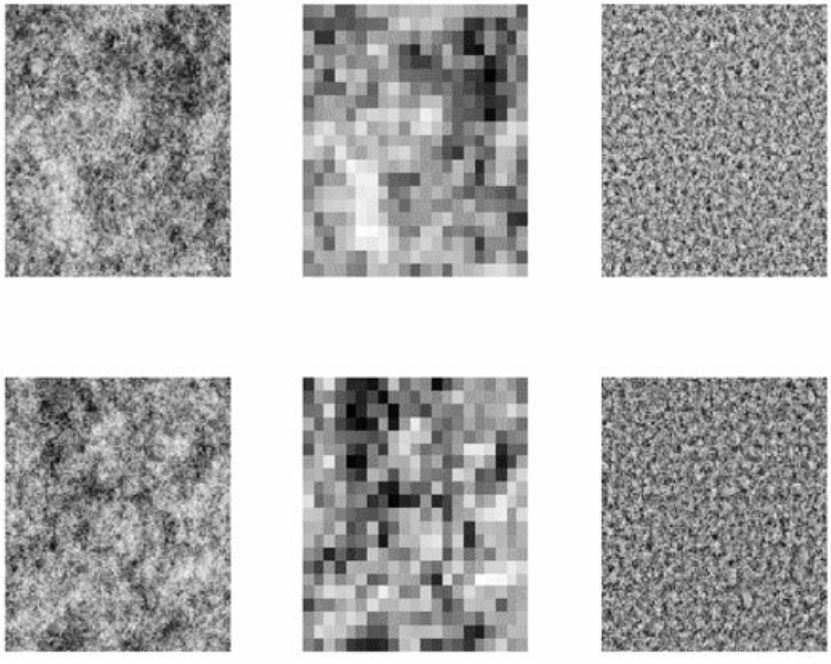

Figure 1. 2-D slices of random spatial noise controlled by the fluctuation statistics of rock observed in borehole logs. (Left) Two sections of 7-octave (spatial frequencies 1–128) spatial fluctuations. (Centre) Three octaves of low-frequency, high-amplitude fluctuations (spatial frequencies 1–8). (Right) Four octaves of high-frequency low-amplitude fluctuations (spatial frequencies 9–128). High-amplitude, low-frequency spatial fluctuations determine the overall structure of the section, while low-amplitude, high-frequency spatial fluctuations are structurally irrelevant. The low-frequency stochastic structure cannot be determined from small-scale sampling of the data cube, and hence efficient production of reservoirs requires measuring of the low-frequency flow structure by direct observation. The numerical distributions provide the elastic property model spatial fluctuations from which to compute the model seismic scattering seismograms.

1.3 Numerical simulation of seismic scattering at stochastic spatial fluctuation structures

Because of the stochastic origin of much reservoir structural complexity, the seismic scattering simulations designed to deal with reservoir complexity are inherently numerical. The realistic simulation of stochastic structures such as reservoir rock requires large model volumes to capture the fluid flow-path connectivity that varies over a large range of spatial wavelengths. Traditional 'effective medium' spatial averaging of rock heterogeneity models is valid only for the right-hand column distributions of Fig. 1, and hence misses the essential reservoir spatial complexity distribution illustrated by the central column.

The 3-D reservoir spatial structures illustrated in Fig. 1 contain approximately 100 spatial frequencies and approximately 4 million scattering elements. The large number of spatial frequencies and scattering elements in such stochastic fluctuation structures requires that numerical simulation of seismic imaging data is computationally efficient. Efficient computation is achieved by approximating the scattering amplitude in terms of a point-scatterer at each location in the data cube. Each point-scatterer amplitude is rapidly computed from the second-order spatial derivatives of the 3-D stochastic fluctuations at that point.

Summation over 3-D point-scatterer distributions with ~ 200 nodes on a side accurately simulates vector seismograms with five octaves of seismogram frequency. For a data cube with 200 nodes on a side, the 32 seismogram frequencies span seismic wavelengths of $\lambda_{\min} \approx 3$ data-cube nodes (needed to define second-order spatial derivatives in the data cube) to $\lambda_{\max} \approx 100$ data-cube nodes (the half-width of the data cube).

A five-octave spectral bandwidth of 32 frequencies is comparable to the best-controlled-source seismic data. In a typical borehole seismic sourcing and sensing configuration, the range of backscattering observation radii extends from $\xi_{\min} \approx 10$ m, as constrained by using model plane waves for scattering dynamics, to $\xi_{\max} \approx 200$ m, as constrained by source power and stability and by sensor ambient noise levels. Scattering seismograms computed for a data cube of a notional 2 m node spacing in a medium with a *P*-wave velocity of $\alpha \sim 3$ m ms^{-1} have frequencies that span the five octaves from 15 to 500 Hz typical of actual borehole seismic sources.

Scattering computations for spherical surfaces embedded in a data cube with ~ 200 nodes on a side sum approximately 4 million numerical scattering amplitudes. With this number of scattering contributions to each seismogram, wideband simulated seismic motion yields robust frequency spectra characteristic of the scattering medium fluctuation statistics. In particular, the present numerical simulations duplicate the $1/t$ amplitude decay and $\sqrt{f}$ spectral enrichment of seismic coda waves in the five-octave frequency band 5–160Hz recorded at a depth of 2.5 km (Leary & Abercrombie 1994a,b).

1.3 Signal-to-noise ratios in time-lapse seismic imaging of heterogeneous reservoirs

In modelling time-lapse seismic images of hydrocarbon reservoirs to distinguish high-flow from low-flow reservoir regions as in Fig. 1, it is necessary to estimate the background scattering

noise level. Consider a seismic scattering seismogram $X(t)$ to be the result of convolving a source wavelet $S(t)$ with an earth structure $E(t)$; that is, $X(t) = S(t)*E(t)$. A subsequent survey can be expressed as

$$X(t) + \Delta X(t) = [S(t) + \Delta S(t)]*[E(t) + \Delta E(t)]\,,$$

for increments $\Delta S(t)$, $\Delta E(t)$, and $\Delta X(t)$ representing changes in, respectively, the seismic source wavelet, the earth structure due to oil–water substitution in a portion of the reservoir, and the seismic survey signal. It follows that the change in the seismic survey signal $\Delta X(t)$ has contributions from changes both in the earth structure $\Delta E(t)$ and in the source wavelet $\Delta S(t)$:

$$\Delta X(t) \approx \Delta E(t)*S(t) + \Delta S(t)*E(t)\,.$$

If the change in source wavelet due to experimental noise is large, then the change in earth structure is obscured and the survey technique is inadequate.

The size of the experimental noise is estimated from the stability of the seismic source $\Delta S(t)$ and the whole-reservoir scattering response $E(t)$ computed by summing seismic backscatters over the entire model volume. At the same time, the target scattering signal $\Delta E(t)$ is computed from scattering at the active reservoir subvolume undergoing oil–water substitution. A method for computing physically accurate estimates of scattering amplitudes represented by $E(t)$ and $\Delta E(t)$ is developed in Section 2.

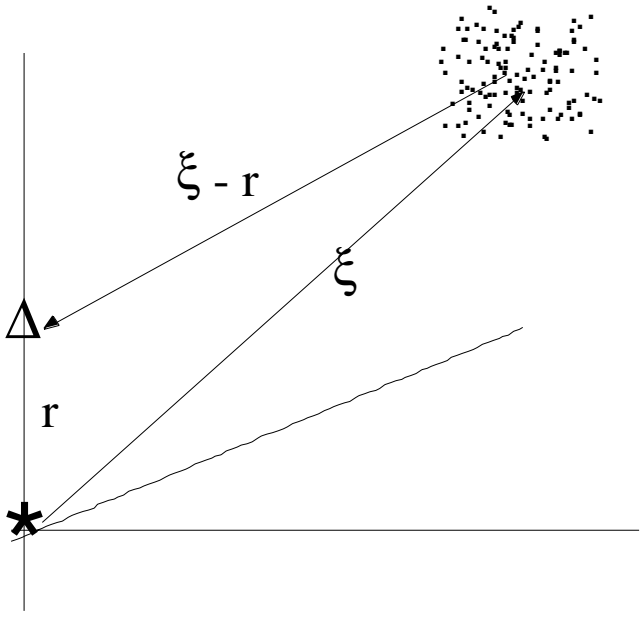

Figure 2. A source (asterisk) of spherically propagating waves is located at the origin of a triaxial coordinate system, and a vector sensor (triangle) is located in a borehole through the origin along the vertical axis at position **r**. A region of point scattering elastic heterogeneities at positions ξ emit a scattered wave that travels to the sensor along the vector $\xi - \mathbf{r}$.

2 FIRST-ORDER BACKSCATTERING FORMALISM FOR HETEROGENEOUS MEDIA

A seismic wave propagating in a non-absorbing but spatially heterogeneous medium is naturally treated in terms of (1) a source pulse which remains unaltered in wave shape despite interactions with the heterogeneities, and (2) scattered waves generated by the source pulse as it encounters heterogeneities in the medium. This is the standard first-order (Born) perturbation approximation to an exact solution (Hudson 1977; Aki & Richards 1980).

The geometry of the source-wave/scattered-wave process is diagrammed in Fig. 2. A disseminated scattering volume is centred about a seismic source at the origin. A seismic sensor at position **r** registers scattered waves from elastic heterogeneities at sites ξ. The source emits a spherically symmetric P or S wave which reaches a scattering volume element ξ at time $t = \xi/\alpha$ or $t = \xi/\beta$. Upon encountering the scattering volume, the source wave generates a secondary spherical wave (either a P or S wave) which reaches the sensor at traveltime $t' = |\xi - \mathbf{r}|/\alpha$ or $t' = |\xi - \mathbf{r}|/\beta$. For P–P and S–S scattering, the total elapsed times of the scattering signal are $t = (\xi + |\xi - \mathbf{r}|)/\alpha$ or $t = (\xi + |\xi - \mathbf{r}|)/\beta$.

In line with the assumption that the source pulse remains unaffected by scattering, it is assumed that scattered waves travel through the medium without themselves being re-scattered. Both source and scattered waves are assumed to be not significantly refracted by smooth velocity trends in the medium. As long as the degree of elastic heterogeneity is small, and/or the total travel path of the source + scattered wave is not too long, the single scattering and constant mean velocity approximations are consistent with borehole sonic velocity log fluctuation magnitudes and trends.

Crustal seismic coda wave scattering data appear to validate the single-scattering approximation for *in situ* applications. Leary & Abercrombie (1994a,b) found that, for earthquake-generated seismic scattering recorded at depth in crustal rock, first-order scattering is a good approximation to at least 150 Hz for shear waves travelling tens of kilometres. The deep-well coda data indicated that multiple scattering became important only for lapse times that far exceed the times relevant to seismic imaging of reservoirs. These data also demonstrate that, compared with intrinsic absorption, scattering is an unimportant mechanism for attenuating seismic waves (Leary 1995).

The deep-well coda wave data are particularly important in validating the first-order scattering approximation applied to the real Earth. *In situ* coda motion is determined by scattering from 3-D distributions of power-law-scaling elastic heterogeneities. Most attempts to compute the validity of the single-scattering approximation are restricted to two dimensions, to scattering distributions determined by a fixed scale-length, and to media with hypothesized rather than observationally constrained intrinsic absorption losses. In view of these very considerable limitations, it is perhaps not surprising that physical models and numerical simulations of seismic coda have left matters somewhat undecided. Dubendorff & Menke (1986) and Frankel & Clayton (1986) found support for first-order scattering approximations. Matsunami (1991), Hoshiba (1991), and Roth & Korn (1993) found that scattering attenuation is negligible compared with intrinsic attenuation. Li & Hudson (1997) concluded from a 2-D scattering simulation that first-order scattering does not account for observed coda wave amplitudes, and suggested that multiple scattering contributions need to be computed. The range of validity of the first-order scattering approximation is thus potentially open to

question. However, deep-well coda data closely paralleling the conditions of numerical simulations undertaken here support the first-order scattering approach to seismic imaging.

2.1 Seismic scatterers as point-force radiators

Seismic scattering amplitudes are computed by combining expressions given by Aki & Richards (1980) for *P*- and *S*-wave point-force radiation vector displacement fields and for point forces generated by heterogeneities in the properties of the material. The point-force terms arise in the first-order scattering approximation to the exact vector wave equation. The scattered wavefield defined by the first-order scattering approximation is a complex amalgam of *P*- and *S*-wave motion over all space. We are initially interested only in that portion of space in which the *P* and *S* waves have separated and for which it is simple to express the complex wave amplitude and phase analytically. In that case we dispense with the complexities inherent in the general first-order scattering solution to the wave equation and simply regard the point-force scatterers as sources of *P* and *S* radiation of magnitude and direction determined by spatially fluctuating material properties with phase given by the source–scatterer traveltime. For narrow-aperture backscattering, one can analytically sum over the infinite frequency bandwidth to define an impulse or δ-function in total traveltime, and to perform a radial integration over the δ-function to define the separated *P*–*P* and *S*–*S* impulse responses of the scattering medium as the sum over all angles subtended by the scattering volume. The angular summation can be efficiently computed for broadband scattering structures representing realistic earth heterogeneity.

Beginning with narrow-aperture backscattering, a point force at the origin is aligned along the 1-axis. The point-force radiation amplitude is specified by (1) the direction cosine $\gamma_1=\partial_1 r=\cos\theta$ relative to the 1-axis, (2) the point-force magnitude $\Im_1$ in Newtons (N) along the 1-axis, and (3) the non-dimensional source-wave time signature $S(t)$. The *P*- and *S*-wave vector displacement $u_i'(\mathbf{r}, t)$ in units of metres registered at time t by a sensor at location $\mathbf{r}$ is

$$u_i'(\mathbf{r}, t) = (4\pi\alpha^2\rho r)^{-1}\gamma_i\gamma_1\Im_1 S(t-r/\alpha) + (4\pi\beta^2\rho r)^{-1}(\delta_{i1}-\gamma_i\gamma_1)\Im_1 S(t-r/\beta)\,, \quad (1)$$

where $\gamma_i=\partial_i r$ fixes the polarization of the motion as a function of sensor position, $r=|\mathbf{r}|$ is the distance between scatterer and sensor, and α and β are the (assumed) uniform *P* and *S* wave speeds of the medium. The contraction $\gamma_i(\delta_{i1}-\gamma_i\gamma_1)=\gamma_1-\gamma_i\gamma_i\gamma_1=\gamma_1-\gamma_1=0$ indicates that the *S*-wave motion is orthogonal to the radial *P*-wave motion. The factor γ_1 indicates that, for a point-force along the 1-axis, the *P*-wave radiation is maximum in the 1-direction ($\cos\theta=1$) and zero along the 2- and 3-axis directions ($\cos\theta=0$). The 1-component of the *S*-wave radiation is proportional to $1-\cos^2\theta$ and is therefore zero along the 1-axis ($\theta=0^\circ$) and maximum along the 2- and 3-axes ($\theta=90^\circ$).

In the present notation, the geometric coordinate system for each scatterer is determined by the source–scatterer axis and the wave polarization. The 1-axis is associated with the direction of source-wave travel, with the 2- and 3-axes transverse to the direction of travel. The spatial variations of the material properties generate radial and transverse derivatives relative to the source–scatterer axis. The radial derivative is expressed equally by ∂_1 or ∂_ξ, and transverse derivatives by ∂_2 and ∂_3. The transverse coordinate axes can be orientated with respect to the polarization of the source *S* wave.

The point-force sources of scattered seismic radiation are found in relation to the source wave by expanding the exact vector wave equation in a two-term perturbation series. The displacement wavefield and material properties are expressed as perturbations (primed symbols) on the uniform (unprimed symbols) elastic constants, $\rho+\rho'$, $\lambda+\lambda'$, $\mu+\mu'$, and on the source field $u_i(\mathbf{r}, t)$ plus the scattered wavefield $u_i'(\mathbf{r}, t)$. The primed scattered wavefield and the spatially variable material property terms are assumed to have magnitudes much smaller than the unprimed source plane wavefield and mean material property terms. Borehole log data indicate that a typical fluctuation is 3 per cent of the mean; it is unusual for fluctuations to exceed 20 per cent of the mean. The exact vector wave equation then partitions into terms defined by known uniform elastic property fields ρ, λ, μ and an unknown scattered wavefield $u_i'(\mathbf{r}, t)$, and terms defined by the known source plane wavefield $u_i(\mathbf{r}, t)$ and the spatially fluctuating elastic parameter fields ρ', λ', μ':

$$\rho\partial_t^2 u_k' - (\lambda+\mu)\partial_k(\partial_j u_j') - \mu\partial_j\partial_j u_k' \approx F_k\,, \quad (2a)$$

$$F_k = -\rho'\partial_t^2 u_k + (\lambda'+\mu')\partial_k(\partial_i u_i) + \mu'\partial_i\partial_i u_k + \partial_k\lambda'\partial_i u_i + \partial_i\mu'(\partial_i u_k + \partial_k u_i)\,. \quad (2b)$$

The secondary source terms F_k have units N m^{-3}. The total scattering motion in the time interval $[t, t+\Delta t]$ is the angular sum over unit volumes $\Delta\xi^3$ in the radial interval $[\xi, \xi+\Delta\xi]=\alpha[t, t+\Delta t]$, where α is the source wave speed.

The point-force radiation wavefield (1) is expressed in terms of a distribution of point-force densities (2b) due to fluctuating material properties ρ', λ', μ' interacting with a source wavefield $u_i(\xi, t)$ of frequency ω. While in practice the source wave diverges from a point, we will assume that the source wave is plane at the point of interaction with the scattering heterogeneity. This approximation can be justified when (1) the scatterer is sufficiently far from the source, (2) the scatterer is sufficiently small, and (3) the source wavelength is sufficiently large that the source wave is effectively planar at the scatterer. It is seen in Section 3.1 that this approximation applies when the source wavelengths and offsets are large compared with the size of the point scatterer $\Delta\xi$. For a *P*-wave velocity $\alpha\approx 4000$ m s^{-1} and material heterogeneity discretization interval $\Delta\xi=1$ m, the source plane-wave approximation works for frequencies below 1000 Hz and for source–scatterer offsets >10 m. Under these restrictions, the only important modification arising from a spherical radiation source is thus the insertion of a geometric attenuation factor $1/\xi$ in the expression for the scattered wave amplitude.

Combining the scatterer response function (1) and scattering excitation function (2b) for a source at the origin and a scatterer at $\boldsymbol{\xi}$, let the wave propagation direction define the 1-axis along the ξ-direction. With the source–scatterer distance $\xi=|\boldsymbol{\xi}|$, *P* waves have polarization [1, 0, 0] with respect to the direction of source-wave propagation, and $u_k^P(\boldsymbol{\xi}, t)\approx S(\omega)\exp[i\omega(t-\xi/\alpha)][1, 0, 0]$, where the source amplitude is in units of metres, $[S(\omega)]=$m. Similarly, *S* waves have polarization [0, 1, 0] or [0, 0, 1]. The source *S* wave is taken to be $u_k^S(\boldsymbol{\xi}, t)\approx S(\omega)\exp[i\omega(t-\xi/\beta)][0, 1, 0]$. From (2b), the *P*- and *S*-wave

secondary scattering point-force amplitudes in units of N m^{-3} are

$$F_k^P \approx [\partial_1(\lambda' + 2\mu'),\, \partial_2\lambda',\, \partial_3\lambda']\partial_1 u^P + [\rho'\omega^2 + (\lambda' + 2\mu')\partial_1^2,\, 0,\, 0]u^P\,, \tag{3a}$$

$$F_k^S \approx [\partial_2\mu',\, 0,\, 0]\partial_1 u^S + [0,\, \rho'\omega^2 + \mu'\partial_1^2,\, 0]u^S\,, \tag{3b}$$

where the unsubscripted scalar variables $u^P = S(\omega)\exp[i\omega(t-\xi/\alpha)]$ and $u^S = S(\omega)\exp[i\omega(t-\xi/\beta)]$ denote the source amplitude and phase along the 1-axis of travel. A wave travelling along the 1-axis encountering heterogeneity distributed along the 1-, 2- and 3-axes thus creates an effective point force proportional to the second radial derivative along the polarization axis (1-axis for *P* waves, 2-axis for *S* waves), with smaller components proportional to the transverse spatial derivatives along the non-polarization axes (2- and 3-axes for *P* waves, 1-axis for *S* waves). Point forces proportional to the spatial derivatives of the material properties and to the temporal and spatial derivatives of the source function mean that high-frequency heterogeneities and source waves create high accelerations and larger-amplitude scattered radiation.

Narrow-aperture seismic backscattering applies when the source and sensor are close and far from the scatterer, $0 < |\mathbf{r}| \ll |\boldsymbol{\xi}|$. Expanding the spatially dependent terms for small values of $\mathbf{r}$ gives $|\mathbf{r}-\boldsymbol{\xi}| \approx \xi - \mathbf{r}\boldsymbol{\xi}/\xi$. In the limiting case of sensor and source at the origin, $|\mathbf{r}-\boldsymbol{\xi}| = \xi$, and the spatial derivatives of (3a,b) reduce to the analytic expressions given in Appendix B:

$$\gamma_i\gamma_k F_k^P = [1,\, 0,\, 0](\rho'\omega^2 - (\omega/\alpha)^2(\lambda' + 2\mu') - i\omega/\alpha\partial_1(\lambda' + 2\mu'))u^P \equiv \gamma_i\gamma_k f_k^P u^P\,, \tag{3c}$$

$$(\delta_{ik} - \gamma_i\gamma_k)F_k^S = [0,\, 1,\, 0](\rho'\omega^2 - (\omega/\beta)^2\mu' - i\omega/\beta\partial_1\mu')u^S \equiv (\delta_{ik} - \gamma_i\gamma_k)f_k^S u^S\,, \tag{3d}$$

where f_k^P and f_k^S denote the point-force vector density in units of N m^{-4} excited by the source-wave displacements u^P and u^S in metres. By this definition, a wave of displacement amplitude u^P or u^S scattering on a heterogeneity of volume $\Delta^3\xi$ is equivalent to a point force of magnitude (3c,d) in newtons.

Using (3c,d) to denote motion at a scatterer at distance ξ due to plane *P* and *S* source waves of frequency ω directed along the 1-axis, eq. (1) gives the backscattered displacement field of frequency ω at the origin for each unit volume of scattering point-force density $f_k(\omega)$:

$$u_i^{PP}(0,\, t|\xi,\, \omega) \approx (4\pi\alpha^2\rho\xi^2)^{-1}\gamma_i\gamma_k f_k^P(\omega)S^0(\omega)\exp[i\omega(t - 2\xi/\alpha)]\,, \tag{4a}$$

$$u_i^{SS}(0,\, t|\xi,\, \omega) \approx (4\pi\beta^2\rho\xi^2)^{-1}(\delta_{ik} - \gamma_i\gamma_k)f_k^S(\omega)S^0(\omega) \times \exp[i\omega(t - 2\xi/\beta)]\,. \tag{4b}$$

The source amplitude $S^0(\omega)$ in (4) is now normalized to a spherical source wave with dimension m^2 per unit frequency ω to accommodate the spherical divergence geometric factor $1/\xi$. As discussed in Section 3.1, at the range of application of (4) a spherical source wave effectively acts on the point scatterer as if it were a plane wave over the dimension $\Delta\xi$ of the scatterer.

Simplifying (4) for *P*–*P* and *S*–*S* backscattering with unit ray vectors $\gamma_i = \gamma_k = [1,\, 0,\, 0]$ gives

$$u_1^{PP}(0,\, t|\xi,\, \omega) \approx (4\pi\alpha^2\rho\xi^2)^{-1}f_1^P(\omega)S^0(\omega)\exp[i\omega(t - 2\xi/\alpha)]\,, \tag{5a}$$

$$u_2^{SS}(0,\, t|\xi,\, \omega) \approx (4\pi\beta^2\rho\xi^2)^{-1}f_2^S(\omega)S^0(\omega)\exp[i\omega(t - 2\xi/\beta)]\,. \tag{5b}$$

In (4) and (5) the scattered wave phase includes both source–scatterer and scatterer–sensor traveltimes $2\xi/\alpha = \xi/\alpha + \xi/\alpha$ and $2\xi/\beta = \xi/\beta + \xi/\beta$. For simplicity, we assume that the source is spherically symmetric about the origin. Summed over the source frequency range and evaluated numerically over successive source-wave shells of dimension $\alpha\Delta t$ encountering the volumetric distribution of scattering elements $\Delta\xi^3$, eq. (4) provides a numerical evaluation of *P*–*P* and *S*–*S* backscattering seismic vector displacement motion $u_k^{PP}(0,\, t)$ and $u_k^{SS}(0,\, t)$, $k = 1,\, 2,\, 3$, in metres.

The vector motion implied by amplitudes (5) refers to a coordinate system fixed to each scatterer. For a general vector seismogram in the overall coordinate system of Fig. 2, the radial *P*-wave motion along the 1-axis and the transverse *S*-wave motion along the 2-axis are geometrically projected onto the fixed geophone coordinate system located at the origin (Fig. 2).

Eqs (3c,d) show that the *P*- and *S*-wave backscattering are identical aside from longitudinal versus transverse polarization and the corresponding moduli and wave speeds. As sonic velocity logs for *P*- and *S*-wave traveltime fluctuations indicate that the spatial fluctuations are highly correlated, it is physically accurate to treat *P*- and *S*-wave scattering on an identical footing provided anisotropy is not being considered. In the following discussion the *P*-wave speed α and polarization are used, but the *S*-wave speed β and polarization can be substituted in the *P*-wave expressions.

2.2 Impulse backscattering response by analytic summation over frequencies

Scattering expressions (5) effectively have finite amplitude for all times t and all spatial points ξ for each wave frequency ω. Relating an impulse of motion at the sensor to impulses of motion at the scatterer and at the source requires summing (5) over all frequencies generated by the source. The simplest source function is the broadband impulse δ-function. The δ-function scattering response is obtained by integrating analytically over an infinite frequency range, retaining only sensor motion (5) at the *P*–*P* total traveltime $t = 2\xi/\alpha$ ($t = 2\xi/\beta$ for *S* waves). As an impulse source has a constant frequency spectrum, the source strength $S^0(\omega) = \text{constant} = S^0$ in units of displacement squared per unit frequency, $[S^0] = \text{m}^2$ s. For an impulse source, the frequency spectrum of the impulse scattering seismogram is directly related to the spatial frequency spectrum of the scattering distribution. The effect of a finite-bandwidth source pulse is found by convolving the impulse scattering response with the band-limited source wavelet.

In the backscattering geometry with the sensor and source at the origin, eqs (5a,b) define the source-wave phase in terms linear in ξ, thus simplifying the relation between frequency integration and the source impulse δ-function. Contracting the

P–P backscattering term (3c) with the backscatter direction cosine $\gamma_k = [1, 0, 0]$ gives

$$\gamma_k f_k^P(\omega) = [i\omega/\alpha\partial_1(\lambda' + 2\mu') - 2\rho\omega^2\alpha'/\alpha],$$

and under frequency integration (5) becomes

$$\begin{aligned}
\mathbf{u}^{PP}(0, t|\xi) &\approx S^0(4\pi\alpha^2\rho\xi^2)^{-1}\int [i\omega/\alpha\partial_1(\lambda' + 2\mu') - 2\rho\omega^2\alpha'/\alpha] \\
&\quad \times \exp[i\omega(t - 2\xi/\alpha)]d\omega \\
&\approx S^0(4\pi\alpha^2\rho\xi^2)^{-1}\{\partial_1(\lambda' + 2\mu') \\
&\quad \times \int i\omega/\alpha \exp[i\omega(t - 2\xi/\alpha)]d\omega \\
&\quad - 2\rho\alpha'/\alpha\int \omega^2 \exp[i\omega(t - 2\xi/\alpha)]d\omega\} \\
&\approx S^0(4\pi\alpha^2\rho\xi^2)^{-1}\{(1/2)\partial_1(\lambda' + 2\mu') \\
&\quad \times \int \partial_\xi \exp[i\omega(t - 2\xi/\alpha)]d\omega \\
&\quad - \rho\alpha^2(\alpha'/\alpha)\int \partial_\xi^2 \exp[i\omega(t - 2\xi/\alpha)]d\omega\} \\
&\approx S^0(4\pi\alpha^2\rho\xi^2)^{-1}\{(1/2)\partial_1(\lambda' + 2\mu')\partial_\xi\delta(t - 2\xi/\alpha) \\
&\quad - \rho\alpha^2(\alpha'/\alpha)\partial_\xi^2\delta(t - 2\xi/\alpha)\}, \qquad (6)
\end{aligned}$$

where displacement $u_1^{PP}(0, t|\boldsymbol{\xi})$ has units of displacement per scattering volume in the direction $\boldsymbol{\xi}$, and the sense of vector motion at the origin is given by direction ξ to each scattering element. The constant S^0 normalizing the source function, $[S^0] = \mathrm{m}^2$ s, can be written $S^0 = u_0 s_0 \tau_0$ in terms of source displacement amplitude u_0 at source dimension s_0 for unit time interval $\Delta t = \tau_0$ characterizing the numerical realization of the δ-function. Radial integration of (6) in the direction $\mathbf{e}_\xi = \boldsymbol{\xi}/\xi$ gives

$$\begin{aligned}
\mathbf{u}^{PP}(t|\mathbf{e}_\xi) &= (1/2)S^0\int \xi^2 d\xi(4\pi\alpha^2\rho\xi^2)^{-1}\{\partial_1(\lambda'+2\mu')\partial_\xi\delta(t-2\xi/\alpha) \\
&\quad - 2\rho\alpha^2\alpha'/\alpha\partial_\xi^2\delta(t - 2\xi/\alpha)\} \\
&= (1/2)u_0 s_0\tau_0(4\pi\alpha^2\rho)^{-1}\int d\xi\{\partial_1(\lambda'+2\mu')\partial_\xi\delta(t - 2\xi/\alpha) \\
&\quad - 2\rho\alpha^2\alpha'/\alpha\partial_\xi^2\delta(t - 2\xi/\alpha)\}. \qquad (7)
\end{aligned}$$

After the radial convolution integral (7), the unit of seismogram displacement at each time interval $\Delta t = \tau_0$ from the scattering area $\xi^2 d\boldsymbol{\Omega} = \Delta^2\xi$ in the direction $\mathbf{e}_\xi$ is $[u_1^{PP}(t|\mathbf{e}_\xi)] = \mathrm{m}$. It remains only to sum over the spatially fluctuating contributions from unit scattering areas of dimension $\Delta^2\xi$.

Spatial convolution of integral (7) can be performed using three δ-function identities. The first two identities are (1) $\delta(F(x)) = \delta(x-a)/|dF/dx|$ with $F(a) = 0$, and (2) $\int dx\, F(x)\delta'(x-a) = -F(a)$. The first identity changes the δ-function variable from a time-variable to a space-variable: $\delta(t - 2\xi/\alpha) \rightarrow (1/2)\alpha\delta(\xi - \alpha t/2)$. By the second identity, performing the radial integration over the first derivative of the δ-function transfers the derivative to the spatially varying elastic parameter factors $\partial_1(\lambda' + 2\mu')$ and α'. The third identity extends the second identity to second-order derivatives of the δ-function:

$$\begin{aligned}
&(3)\int dx F(x)\delta''(x - a) \\
&\quad = \int dx[F(x)\delta'(x - a)]' - \int dx F'(x)\delta'(x - a) \\
&\quad = [F(x)\delta'(x - a)]|_{-\infty}^{+\infty} + F''(a) = F''(a).
\end{aligned}$$

Applying identities (1) to (3) to eq. (7) and incorporating the normalization factor $(\rho\alpha^2)^{-1}$ into the integrand yields

$$\begin{aligned}
&\mathbf{u}^{PP}(t = 2\xi/\alpha|\mathbf{e}_\xi) \\
&\quad = \alpha/4u_0 s_0\tau_0(4\pi\alpha^2\rho)^{-1}\{\partial_1^2(\lambda' + 2\mu') - \rho\alpha^2\partial_1^2(\alpha'/\alpha)\}|_{\xi=\alpha t/2}(\mathbf{e}_\xi) \\
&\quad = \alpha u_0 s_0\tau_0/16\pi\partial_1^2\{\lambda' + 2\mu')/(\lambda + 2\mu) - \alpha'/\alpha\}|_{\xi=\alpha t/2}\mathbf{e}_\xi \\
&\quad = \alpha u_0 s_0\tau_0/16\pi\partial_1^2\{\rho'/\rho + 2\alpha'/\alpha - \alpha'/\alpha\}|_\xi\mathbf{e}_\xi \\
&\quad = \alpha u_0 s_0\tau_0/16\pi\partial_1^2\{2\alpha'/\alpha - \rho'/\rho\}|_\xi\mathbf{e}_\xi \qquad (8)
\end{aligned}$$

with the directional unit vector indicating the sense of backscattered motion at the origin. Using angled brackets $\langle\ \rangle$ to denote angular summation over all directions $\mathbf{e}_\xi$, the total vector *P–P* backscattered vector motion at the origin can be written as

$$\mathbf{u}^{PP}(t = 2\xi/\alpha) = \alpha u_0 s_0\tau_0/16\pi\langle\partial_1^2\{2\alpha'/\alpha - \rho'/\rho\}|_\xi\mathbf{e}_\xi\rangle, \qquad (9a)$$

where motion for the scattering volume in each direction $\mathbf{e}_\xi$ is projected onto the sensor coordinate axes $i = 1, 2, 3$. The wave speed α in (9a) controls the temporal interval over which scattered waves contribute to the amplitude registered at time t. Accordingly, α is expressed in $\mathrm{m}/\Delta t$, where Δt is the temporal discretization interval of the displacement seismogram. A useful value of Δt is 1 ms, and a nominal value of the wave speed α is 4 m ms^{-1}. The units of wave speed α are immaterial for the normalized fluctuation term α'/α.

Eq. (9a) indicates that the temporal spectra of backscattering seismograms scale as the angular average over the second radial derivative of material property fluctuations in the surrounding rock mass. The total scattering amplitude can vary as a function of time t as the random backscatterings of the outgoing spherical wave interfere at the origin. The overall magnitude and time-behaviour of (9a) are not apparent in the given form. Apart from the effect of angular averaging over multiple sources of scattering heterogeneity, however, the second spatial derivative of fluctuations in (9a) means that the amplitude spectrum of motion $u_i^{PP}(t = 2\xi/\alpha)$ scales as ω^2 and the power spectrum scales as ω^4. Eq. (9a) thus expresses the plane wave Rayleigh scattering frequency dependence (e.g. Aki & Richards 1980).

2.3 Numerical evaluation and normalization of the angular sum scattering amplitude

Because (9a) cannot be expressed analytically, the magnitude and time behaviour of the total scattered motion is computed numerically from (9c) below for random distributions of scatterers with a specific power-law-scaling behaviour. The numerical summation is carried out over a Cartesian grid with discretization interval $\Delta\xi$ and volume element $\Delta^3\xi$. For numerical purposes the δ-function converts to a finite time interval $\Delta t = \Delta\xi/\alpha$ and integration goes to summation over scattering areas $\Delta^2\xi$ of thickness $\Delta\xi = \alpha\Delta t = \alpha\tau_0$:

$$\mathbf{u}^{PP}(t = 2\xi/\alpha) \approx \alpha u_0 s_0\tau_0/8\pi\,\Sigma_{ijk}\,1/\xi^2\{\partial_\xi^2(\alpha'/\alpha - \rho'/2\rho)\mathbf{e}_\xi\}_{ijk}\Delta^2\xi. \qquad (9b)$$

The three grid summation indices i, j and k are constrained to two angular degrees of freedom at time $t=2n\Delta\xi/\alpha$ by the condition $\xi^2=\Delta\xi^2 n^2$, $n^2=(i^2+j^2+k^2)$, and $\mathbf{e}_\xi$ is the radial unit vector. At each time interval centred on time $t=2n\Delta\xi/\alpha=2\xi/\alpha$, the geometrical spreading term $1/\xi^2$ can be factored from the sum to appear as the scattered wave amplitude pre-factor $(s_0/\xi)(\alpha\tau_0/\xi)=(s_0/\xi)(\Delta\xi/\xi)$, thus normalizing geometric spreading to the effective size of the source s_0 and the effective size of the unit scattering volume $\Delta\xi=\alpha\tau_0$. The unit area factor $\Delta^2\xi$, is incorporated into the sum, rendering the summand non-dimensional as the numerical derivatives are taken at finite increment $\Delta\xi$, $(4\pi)^{-1}\,\Sigma_{ijk}\{\partial_\xi^2(\alpha'/\alpha-\rho'/2\rho)\Delta^2\xi\}_{ijk}$. The factor 4π (steradians) normalizes the angular integral to unity over a unit sphere. Vector scattering motion at time t, $\mathbf{u}^{PP}(t=2n\Delta\xi/\alpha)$, thus reduces to effectively dimensionless factors expressing geometric scaling of the source and backscattered waves and the scattering amplitude of the spatially fluctuating medium:

$$\mathbf{u}^{PP}(t=2n\Delta\xi/\alpha)\approx u_0(s_0/\xi)(\Delta\xi/\xi)\times(4\pi)^{-1}\Sigma_{ijk}\{[\partial_\xi^2(\alpha'/\alpha-\rho'/2\rho)\Delta^2\xi]\mathbf{e}_{ijk}\}_{ijk}\,. \tag{9c}$$

It is understood in (9c) that the vector motion at the origin is the resultant of summing over weighted directional unit vectors $\mathbf{e}_{ijk}$ pointing to the scattering element at location (i, j, k). Accounting for notational differences, space-differentiation versus time-differentiation, and spherical versus plane source waves, (9c) agrees with the plane-wave backscattering expressions of Li & Hudson (1997).

To establish the numerical robustness of the summation in (9c), consider the bracketed fluctuation terms in (9c) to be fixed at unity and independent of an implied sign of radial motion at the origin. Fig. 3 shows that the summation term of (9c) yields values $\approx 4\pi$ for spherical shells of radius $>10\Delta\xi$, indicating that the scattering integral (9c) is numerically accurate for scattering radii as low as 10 grid units $\Delta\xi$. The scattering simulations given below observe this limit on inner scattering radius. It is shown in Section 3.1 that a scattering radius of 10 grid units $\Delta\xi$ is consistent with a plane-wave approximation for the spherical source wave encountering scattering elements of dimension $\Delta\xi$.

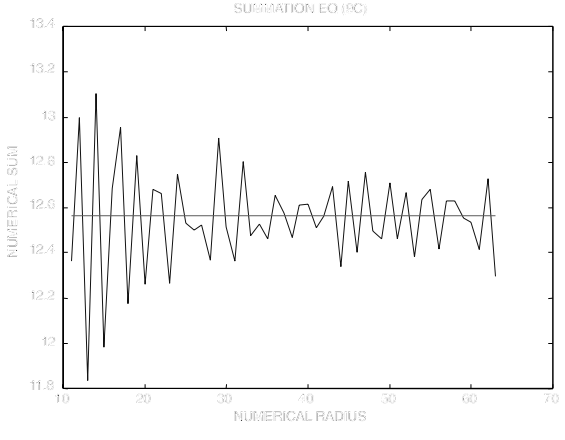

Figure 3. The fluctuating trace is the amplitude of the eq. (9c) summation for unity summand compared with the analytic value 4π given by the straight line for successive spherical radii in units of data-cube node spacing $\Delta\xi$. The mean value of the fluctuating trace indicates that the scattering amplitude (9c) is properly normalized at numerical radii >10 grid units $\Delta\xi$.

2.4 Angular averaging of the backscattering impulse response

Angular averaging over random elastic heterogeneities determines the backscattered seismogram amplitude (9c) and its Fourier spectrum. Although the elastic heterogeneities are spatially correlated noise, the fluctuations are not symmetric or in general spatially correlated across the diameter of the source wave front. The effect of angular summation can be understood in terms of uncorrelated randomness between the amplitude and sign of diametrically opposed scatterers. Scattering fluctuations of material properties seismic velocity and/or mass density tend to have zero mean value about the constant background velocity and density of the reservoir rock. That is, in any spatial direction there are equal numbers of positive and negative fluctuations in the fluctuating elastic properties of the reservoir. Furthermore, the variance of uncorrelated random sample mean decreases with increasing sample size. We can thus expect that (1) the angular summation (9c) tends to zero for any two diametrically opposed scattering directions, and (2) the approach to zero is closer and closer for increasing traveltime; hence (3) since for any total traveltime there are more scatterers at higher frequencies than at lower frequencies, higher-frequency scattering tends to zero faster than lower-frequency scattering.

These expectations for the angular summation (9c) of scattering amplitudes can be quantified in terms of rms amplitudes of seismic motion at the sensor. For summation over uncorrelated spatial fluctuations giving rise to backscattered seismic motion at the sensor, the rms amplitude will tend to be suppressed by a factor $1/\sqrt{N}$ for N fluctuations contributing to motion at any arrival time $t=2\xi/\alpha$. As the number of backscattering fluctuations from a subarea $\xi^2 d\Omega$ is determined by the wavelength, shorter wavelengths sample larger numbers of fluctuations than longer wavelengths. Accordingly, higher frequencies detect greater numbers of spatially uncorrelated fluctuations than do lower frequencies, hence the number of backscattered fluctuation phases $N\propto\omega^2$. The statistics of uncorrelated randomness imply that, relative to plane-wave Rayleigh scattering, the amplitude and the spectra of spherically sourced and scattered seismic motion in a random scattering medium is suppressed inversely with time and with frequency, $1/\sqrt{N}\propto 1/t$ and $1/\sqrt{N}\propto 1/\omega$.

The analysis of scattered wave spectra may be further quantified in terms of the spatial correlation of random media. If random material parameter fluctuation power spectra scale as f^B, the spatial fluctuation amplitude spectra scale as $f^{B/2}$, and scattered wave frequency spectral scaling will be affected in proportion to the exponent $B/2$ (e.g. Turcotte 1992; Leary 1997). The second derivatives of (9c) enhance the higher scattered frequencies to scale as $f^{B/2+2.}$, and the $1/f$ suppression factor from angular averaging of backscattered seismic motion is expected to yield seismograms with amplitude spectra scaling as $f^{B/2+1.}$ When $B=-1$, typical of rock (Leary 1991, 1997, 1998), the resulting seismogram spectral amplitudes scale as $\sqrt{f}$. At the same time, the angularly uncorrelated nature of random fluctuations reduces the scattered wave amplitude as a function of traveltime, $1/t$. Summation over random scatterers thus

agrees with the $\sqrt{f}$ spectral power-law enrichment of coda wave amplitude spectra and $1/t$ amplitude decay seen by Leary & Abercrombie (1994a,b).

3 MODEL VALIDATION: BACKSCATTERING SPECTRA AS FUNCTIONS OF SCATTERING MEDIUM FLUCTUATION STATISTICS

The angular summation of uncorrelated random fluctuations about the expanding sphere of a source wave implies (Section 2.4) that the backscattered wave motion has rms amplitude decaying as $1/t$, and has a power-law spectral amplitude that scales as $f^{1+B/2}$ when scattered by a medium with fluctuations having Fourier spectral power that scales as f^B. For $B=-1$, characteristic of crustal rock, it is expected that the spectrum of a backscattered impulse wavelet will scale as $\sqrt{f}$. These expectations are tested for a range of values of the spatial fluctuation scaling exponent B by numerically summing (9c) over successive spherical source wave surfaces embedded in 3-D data cubes characterized by power-law spatially correlated random fluctuations. Scattering in a medium characterized by a fixed scattering length a is also simulated.

3.1 Scattering data cube

Numerical realizations of backscattering expression (9c) are computed for a 3-D grid or data cube of random numbers with the source and sensor at the centre. Fig. 1 shows slices of such a data cube. A data cube with 200 numbers on a side is feasible on a standard PC using, for instance, the Matlab numerical package (Matlab 2000). Each grid-point random number represents the mean material property of a 1 m cube. The numerical scattering simulation then corresponds to borehole-sourced and sensed field data at ranges up to a radius of 100 m. For a P-wave velocity of 4000 m s^{-1}, a 4 m wavelength corresponds to 1000 Hz, and a 100 m wavelength corresponds to 40 Hz.

For frequencies near 1000 Hz, a spherical wave of radius 10 m and wavelength 4 m begins to appear as a plane wave to a 1 m scattering element. This follows because a spherical and a plane wave cannot be distinguished if the phase and amplitude do not vary significantly over the spatial dimension $\Delta\xi$. The amplitude difference between successive spherical and plane waves is $\approx\Delta\xi/\xi$. For a plane wave $\exp[ik\xi]$, the phase is identical at two laterally adjacent points $[\xi, 0, 0]$ and $[\xi, \Delta\xi, 0]$, whereas a spherical wave is phase-shifted $\approx(1/2)k\Delta\xi^2/\xi$ between the two points. For source–scatterer offsets $\xi>10$ m such that $\Delta\xi/\xi<10^{-1}$, and for wavelengths such that $\pi\Delta\xi/\lambda<1$, the difference between the plane wave and spherical wave interaction with the medium is small and may be neglected. We may then understand numerical simulations in terms of field observations in the frequency range 40 to 1000 Hz for a spherical volume of radius between 10 and 100 m where the medium is specified in terms of fluctuations over spatial intervals of 1 m. For modelling a lower range of frequencies or larger crustal volumes, unit cubes with $\Delta\xi=2$–25 m shift the observation frequency range to 15–500 Hz and 1–40 Hz for volumes 400 m to 5 km on a side.

At each grid point in the data cube, the radial second derivative of the random fluctuations is computed. The computed radial displacement is projected onto the grid axes along the radius vector $\mathbf{e}_\xi$ to define the x-, y- and z-axis sensor displacement motion $u_i^{PP}(t=2\xi/\alpha)$ at two-way traveltime $t=2\xi/\alpha$. The radial derivative of fluctuation property $M(x, y, z)$ at grid point $[x, y, z]$ is the directional derivative

$$\partial_\xi M(x, y, z) = \partial_x M\partial_\xi x + \partial_y M\partial_\xi y + \partial_z M\partial_\xi z\,.$$

Since

$$[x, y, z] = \xi[x/\xi, y/\xi, z/\xi] = \xi[\gamma_x, \gamma_y, \gamma_z] = \xi\mathbf{e}_\xi\,,$$

the first directional derivative can be written $\partial_\xi M(x, y, z) = \mathbf{e}_\xi\cdot\nabla M$. For the second radial derivative,

$$\partial_\xi^2 M(x, y, z) = \partial_\xi(\mathbf{e}_\xi\cdot\nabla M) = (\mathbf{e}_\xi\cdot\partial_\xi\nabla M) = \mathbf{e}_\xi\cdot\nabla\partial_\xi M$$

$$= \mathbf{e}_\xi\cdot\nabla(\mathbf{e}_\xi\cdot\nabla M) = \gamma_x^2\partial_x^2 M + \gamma_y^2\partial_y^2 M + \gamma_z^2\partial_z^2 M\,.$$

The numerical second derivatives along the discrete grid axes are $\partial_x^2 M \equiv [M(x-\Delta x, y, z) + M(x+\Delta x, y, z) - 2M(x, y, z)]/\Delta x^2$, etc.

The fluctuation statistics of the scattering data cube are controlled by weighting the radial wavenumber in the 3-D FFT transform domain of a 3-D array of Gaussian-distributed (uncorrelated, independent or white) random numbers (Turcotte 1992). For power-law-scaling fluctuation statistics, the wavenumbers are radially filtered by a simple power law in radial wavenumber. In order to impose a correlation length on the data-cube fluctuations, the power-law filter is applied only to frequencies for wavelengths smaller than the correlation length a. The data-cube fluctuation statistics are validated by the condition that numerical boreholes drilled through the data cube return spatial frequency spectra with the correct exponent, or that for a medium with correlation length a the spectrum is power-law above $1/a$ while flat below $1/a$.

A sample three-component displacement seismogram computed with (9c) is shown in Fig. 4 for an earth-model data cube with power-law spectral scaling exponent $B=-1$. The elastic constants fluctuate with 3 per cent standard deviation about their whole sample mean; the mean P-wave velocity is 4 m ms^{-1}. The seismic displacement amplitude falls off inversely with seismic traveltime, as observed in deep borehole recordings of seismic coda waves (Leary & Abercrombie 1994a,b).

3.2 Scattering seismogram spectra

Fig. 5 summarizes the backscattered wave spectral results for values of spatial scaling noise exponent B between 0 and 2.5. Sample numerical vector-displacement seismograms (9c) and their amplitude spectra are shown in Figs 6 to 8. These figures show the power-law frequency scaling behaviour for the scattered wave spectra computed for a range of f^B-scaling-noise media. The principal categories of power-law-scaling spatial fluctuations are determined by three integer scaling exponents. Each scaling exponent is characteristic of numerous physical and engineering phenomena (Mandelbrot 1983, 1999): (1) $B\approx 0$, generating spatially uncorrelated fluctuations ('white noise'); (2) $B\approx -1$, generating moderately spatially correlated fluctuations as observed in crustal rock ('$1/f$-noise'); and (3) $B\approx -2$, generating strong spatially correlated fluctuations as observed in many physical systems ('Brownian noise'). Figs 9 and 10 illustrate numerical vector-displacement seismograms and corresponding spectra for data cubes simulating a medium dominated by a narrowband correlation length a. The

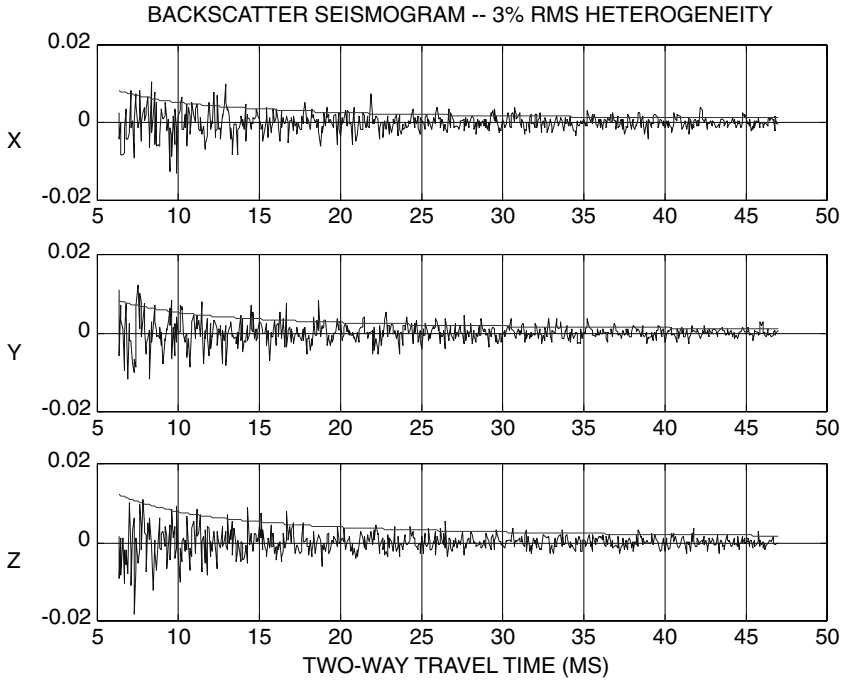

Figure 4. Synthetic displacement seismic motion computed with (9c) rms fluctuation $\langle \alpha'/\alpha \rangle = 3$ per cent and mean *P*-wave velocity $\alpha = 4$ m ms^{-1}; curves show that the seismic amplitudes fall off inversely with traveltime.

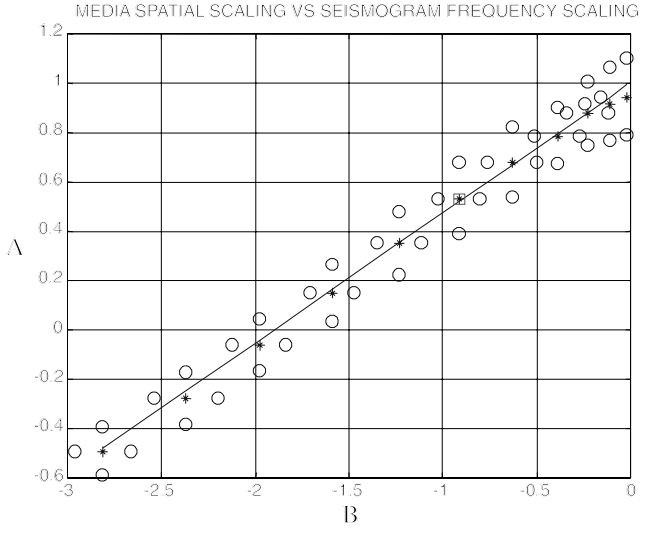

Figure 5. Plot of the numerically determined relation between exponent B controlling the scaling character of the spatial fluctuations of a 192-node data cube (horizontal axis), and the scaling exponent characterizing the temporal spectra of scattering seismograms (vertical axis). The plot summarizes 15 data-cube realizations for each value of B. Asterisks locate the mean of (i) the scaling exponent determined by the spatial fluctuation power spectra of 'numerical boreholes' through the data cubes, and (ii) the scaling exponent determined from the amplitude spectra of the scattering seismogram vector motion. Rms deviations from the mean scaling exponent B are denoted by horizontally offset o's about each asterisk; rms deviations from the mean amplitude spectral scaling exponent of scattering seismograms are denoted by vertical error o's. The straight line denotes the expected $B/2+1$ dependence of the scattering seismogram spectral scaling exponent on the scattering medium scaling exponent. The asterisk in a square denotes simulations relating $1/f$-noise fluctuations recorded in well logs to deep-well coda spectra (Leary & Abercrombie 1994a,b).

character of the seismograms varies rapidly as the aperture of temporal frequencies moves across the narrow spatial frequency aperture of correlation structure.

Fig. 5 shows that the synthetic seismograms yield amplitude spectra scaling exponent values $1+B/2$, in systematic agreement with the data-cube spatial fluctuation power-law-scaling exponent B deduced in Section 2.4. The values of spatial fluctuation scaling exponents, denoted by asterisks, are averages over 15 data-cube realizations. The horizontal error o's give the standard deviation from the mean B for the 15 data cubes. The vertical error o's give the standard deviation from the mean of temporal amplitude spectral scaling exponents for three components of vector motion as shown in Figs 6 to 8.

The assumed flat or white-noise spectrum of the δ-function source pulse $S(\omega) = S_0 =$ constant means that the spectra of the simulated backscattered motion shown in Figs 6 to 8 directly relate to the fluctuation statistics of the scattering volume. The sample synthetic scattering seismogram spectra have the power-law spectral behaviour expected from (9c) and observed *in situ* for the deep-well coda seismograms (Leary & Abercrombie 1994a,b). The seismogram spectra are shown for a bandwidth of 60 frequencies, but only the first 32 frequencies carry scaling information about the data-cube spatial correlation spectrum. Higher frequencies contain uncorrelated random information since the data cube has no structural information at wavelengths shorter than three nodes. Accordingly, the slope of the seismogram amplitude spectra are determined only for the first 32 frequencies.

Two scattering simulations for media characterized by a fixed scale-length a are shown in Figs 9 and 10. The correlation length a parametrizes an exponential spatial correlation function $\exp[-(r/a)^2]$. The corresponding spatial frequency filter for the data cube is $\exp[-(ka)^2]$, where $k = nk_0$ are successive spatial frequency overtones of the fundamental spatial frequency for a

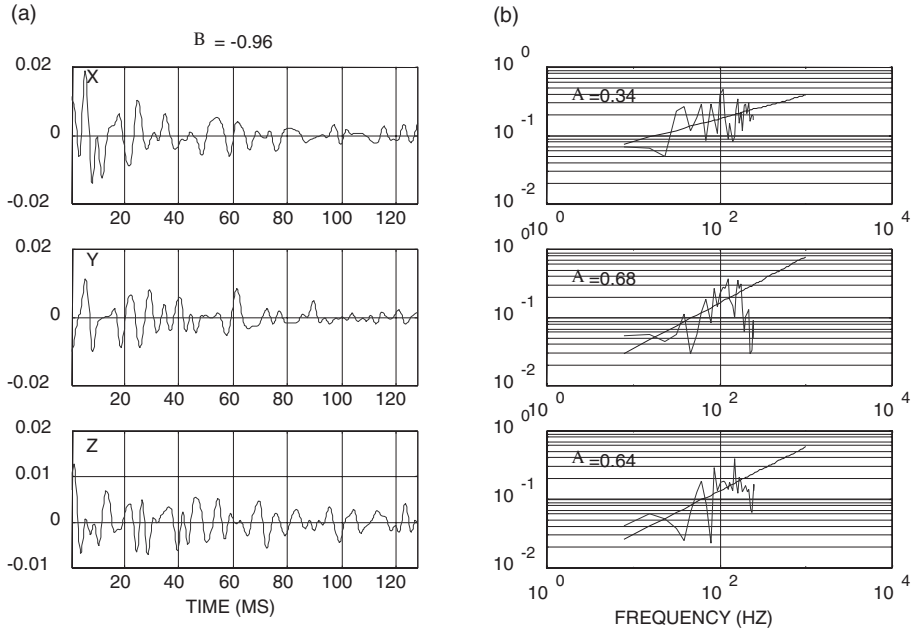

Figure 6. (a) Components of vector displacement motion at the centre of a 192-node data cube given by (9c) for spatial fluctuation scaling exponent $B \approx -1$. (b) Amplitude spectra of opposing seismograms; the power-law slope of the amplitude spectra is given by the straight-line fit on a log–log plot for the first 32 frequencies.

data cube of N_{dc} nodes, and $k_0 = 2\pi/L$ with $L = N_{dc}\Delta L/2$ the scale-length of the data cube, and overtone index n ranging from 1 to $N_{dc}/2$.

Figs 9 and 10 show the effects on scattering spectra as the correlation length a is varied with respect to the data-cube size L. If the correlation length a is small compared with L, the filter $\exp[-(ka)^2]$ is negligible for all or most spatial frequencies, and the medium fluctuation statistics revert to uncorrelated randomness to yield scattering seismogram amplitude spectra that scale with the exponent 1 expected from spatial scaling exponent $B = 0$. If a is large compared with L, the filter acts to diminish the scattering amplitude so that the scattering signal is negligible.

The appearance in Figs 9 and 10 of the peak in spectral scattering amplitude at the expected frequencies shows that the computed scattering responds to the correlation length built into the data cube. This dependence, the systematic relation between spatial fluctuation spectral scaling exponent B and temporal spectral scaling exponent $1 + B/2$ seen in Figs 5 to 8, and the $1/t$ amplitude decay of the backscattered seismic motion,

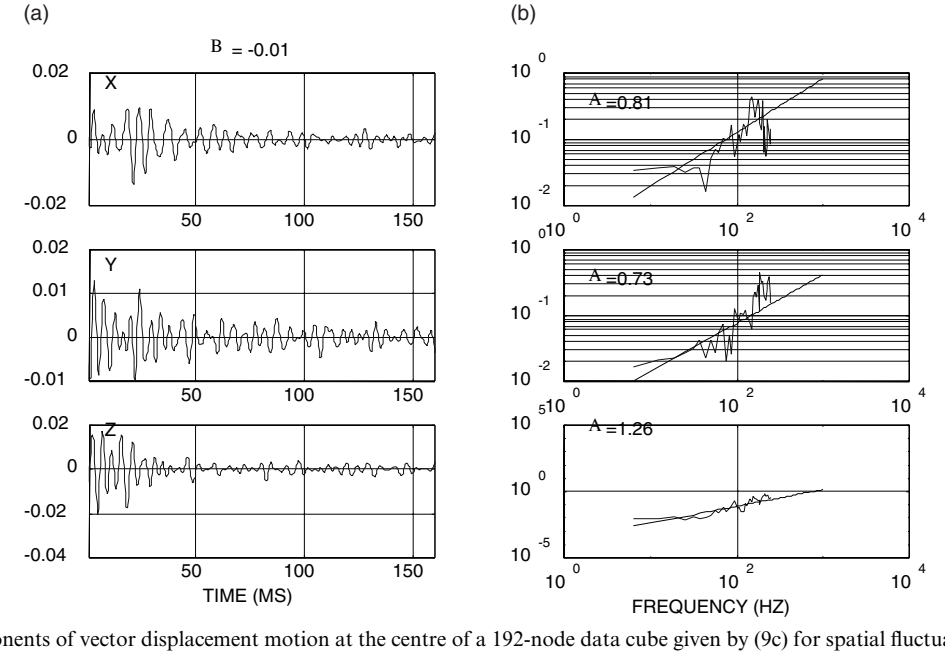

Figure 7. (a) Components of vector displacement motion at the centre of a 192-node data cube given by (9c) for spatial fluctuation scaling exponent $B \approx 0$. (b) Amplitude spectra of opposing seismograms; the power-law slope of the amplitude spectra is given by the straight-line fit on a log–log plot for the first 32 frequencies.

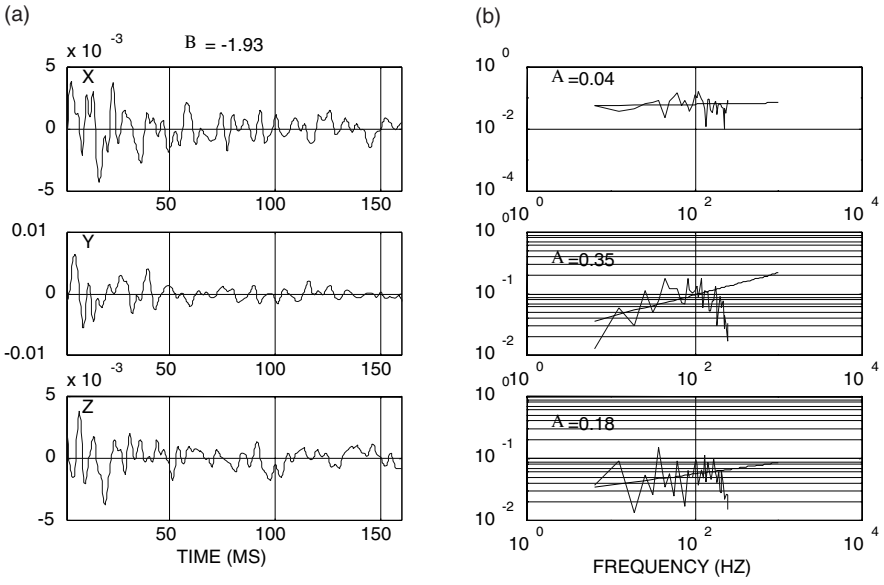

Figure 8. (a) Components of vector displacement motion at the centre of a 192-node data cube given by (9c) for spatial fluctuation scaling exponent $B \approx -2$. (b) Amplitude spectra of opposing seismograms; the power-law slope of the amplitude spectra is given by the straight-line fit on a log–log plot for the first 32 frequencies.

validate the scattering expression (9a) and its numerical implementation (9c). These expressions are now used to simulate time-lapse scattering and multi-offset static imaging in the single-well borehole seismic geometry using sources and sensors in the same well.

4 TIME-LAPSE BOREHOLE SEISMIC IMAGING OF HETEROGENEOUS RESERVOIRS

Extensive well-log evidence in sedimentary rock (Leary 1997, 1998; Leary & Al-Kindy 2002) indicates that the $B = -1$ ($1/f$-noise) class of data cubes can be used as a standard physical earth model for simulating time-lapse and static seismic imaging data in the single-well source–sensor geometry of Fig. 2. In particular, a $1/f$-noise earth model can be combined with (9c) to estimate the source signal-to-noise level and stability needed for time-lapse seismic imaging of active hydrocarbon reservoirs, and the source signal-to-noise level and sensor density needed to form static seismic images of subsurface structures.

Time-lapse seismology using the single-well geometry of Fig. 2 can detect signals from spatially and temporally localized earth events if three criteria are met:

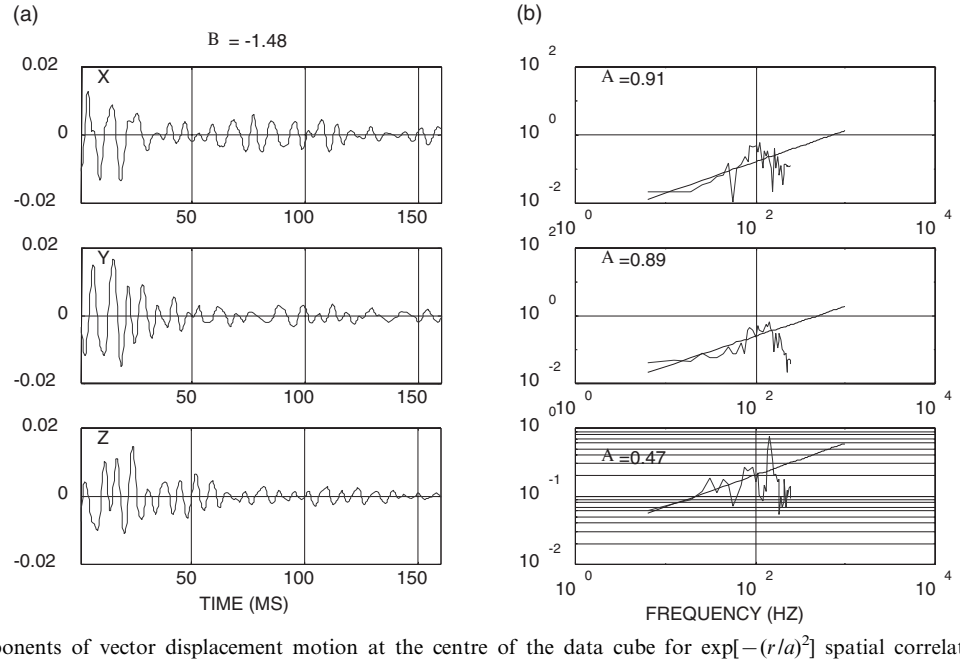

Figure 9. (a) Components of vector displacement motion at the centre of the data cube for $\exp[-(r/a)^2]$ spatial correlation with correlation parameter $a = 1/3$ the size of the data cube. (b) Amplitude spectra of opposing seismograms.

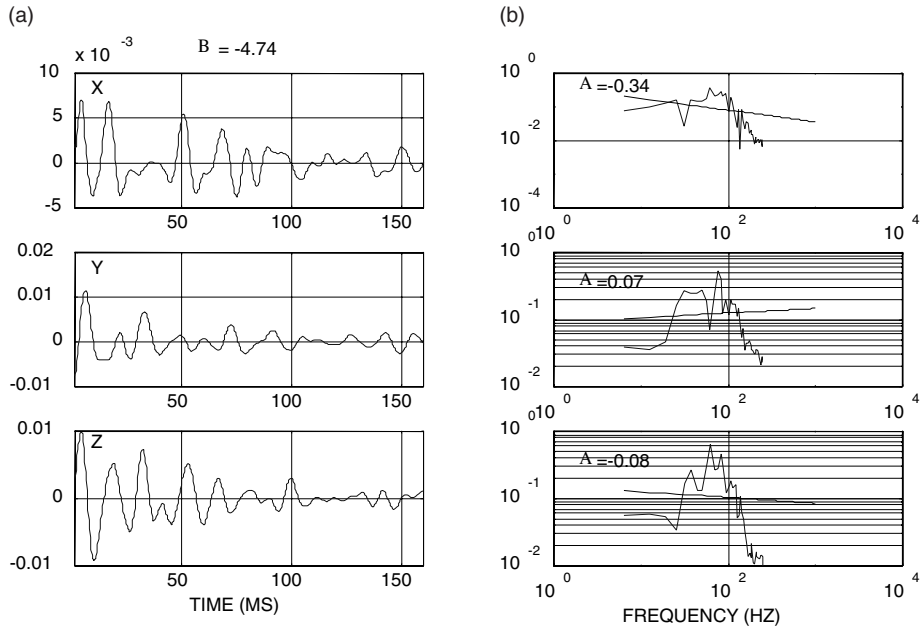

Figure 10. (a) Components of vector displacement motion at the centre of the data cube for $\exp[-(r/a)^2]$ spatial correlation with correlation parameter $a=1/\sqrt{3}$ the size of the data cube. (b) Amplitude spectra of opposing seismograms.

(1) the source and sensor are sufficiently stable that the residual seismic scattering motion from differencing successive illuminations of the static background earth structure does not obscure the physical time-lapse signal;

(2) the time-lapse volume is sufficiently spatially localized that backscattered vector motion can be interpreted uniquely as coming from a specific location;

(3) the backscattered signal is larger than uncorrelated random seismic noise in the earth and instrument noise in the recording system.

These three borehole seismic imaging criteria are modelled with backscattering formulation (9c) for a $1/f$-noise fluctuating reservoir structure constrained by well-log and well-core observations, and using empirical amplitude and stability data from the particular borehole seismic source.

4.1 Background noise from source and sensor instability

Time-lapse imaging noise arises from the static scattering background because no actual source and sensor system is exactly reproducible. Changes in the source wavelet and sensor response produce residual seismic motion that can mask a time-lapse signal when the two survey seismograms are differenced. A particular borehole seismic source, the downhole orbital vibrator (DOV), has been demonstrated to generate a source pulse stable to a few parts in 10^4 (SMSITES 2001). This means that in principle one can detect a time-lapse signal if the size and elastic property changes of an active reservoir volume return a backscattering signal that is, say, $5/10^4$ of the amplitude of the whole-reservoir static backscattering.

The time-lapse seismic monitoring signal is a partial sum (9c) of point-force scatterers over a localized volume hosting the time-dependent change in earth properties. In $1/f$-noise distributions recorded in a North Sea oil reservoir, high porosity is spatially associated with high fluid permeability (Leary & Al-Kindy 2001). Volumes of high-amplitude porosity fluctuation are hence likely to host significant fluid-flow events such as oil–water substitution. The substitution of water for oil in regions of high porosity/permeability creates a change in elastic properties that is of the order of the static elastic property fluctuations. Laboratory data on *P*-wave speeds, for instance, suggest that $5<\alpha'/\alpha<15$ per cent for oil–water substitution (Wang & Nur 1992). As a guide to the magnitude of a time-lapse seismic scattering signal from fluid substitution, it will be assumed that the oil–water substitution changes the local elastic properties by an amount comparable with the 3 per cent fluctuation amplitude commonly observed in local $1/f$-noise distributions measured by well logs and well-core sequences.

For the time-lapse seismic scattering simulation, consider a reservoir volume at radius $n\Delta\xi$ with characteristic dimension $m\Delta\xi$ in units of the data-cube node spacing $\Delta\xi$. The active reservoir volume is bounded by radii $(n-m/2)\Delta\xi$ and $(n+m/2)\Delta\xi$ and subtended by solid angle $\Delta\Omega\approx\pi(m/2n)^2$. The time-lapse scattering amplitude (9c) for the volume is

$$\mathbf{u}^{\mathrm{TL}}(t=2n\Delta\xi/\alpha)$$

$$\approx u_0(s_0/\xi)(\Delta\xi/\xi)(1/4\pi)\,\Sigma_{ijk}\{[\partial_\xi^2(\alpha'/\alpha-\rho'/2\rho)\Delta^2\xi]\mathbf{e}_{ijk}\}_{ijk},$$

$$(n-m/2)\Delta\xi<\xi<(n+m/2)\Delta\xi, \qquad (10)$$

where the summation over scattering nodes designated by indices i, j, k is constrained by $\xi^2=\Delta\xi^2n^2$, $n^2=(i^2+j^2+k^2)$ for the given range of radius ξ and by solid angle $\Delta\Omega\approx\pi(m/2/n)^2$ in a specific direction. The static background seismic wavefield $\mathbf{u}^{PP}(t)$ shown in Figs 5 to 10 is computed by summing the point-force contributions (10) over 4π steradians of solid angle for the heterogeneous reservoir volume surrounding the source–sensor system.

If two time-lapse survey source pulses differ slightly, the source difference $\Delta S(t) = S_1(t) - S_2(t)$ convolved with the whole-reservoir seismic scattering response $\mathbf{u}^{PP}(t)$ gives the residual background wave motion, $\Delta\mathbf{u}_i^{PP}(t) = \Delta S(t) * \mathbf{u}_i^{PP}(t)$. The size of the time-lapse scattering signal $\mathbf{u}_i^{\mathrm{TL}}$ relative to the static scattering background noise $\Delta\mathbf{u}_i^{PP}$ must be greater than 1:

$$\mathrm{S/N} \approx |\mathbf{u}_i^{\mathrm{TL}}| / |\Delta\mathbf{u}_i^{PP}| > 1 \qquad (11)$$

as a condition for detecting fluid-substitution events as in, say, a producing hydrocarbon reservoir.

Figs 11 to 13 illustrate the time-lapse seismic imaging computation. Fig. 11 displays a section of a $1/f$-noise data cube having a high-porosity and a correspondingly high-permeability spatial trend as implied by poroperm well-core data (Leary & Al-Kindy 2001). The permeability pathway of Fig. 11 connects data-cube nodes having above-threshold permeability. In a uniform geofluid pressure field, fluid would flow along the connectivity structure defined by the high-porosity, high-permeability nodes. Material constants are associated with the high-porosity, high-permeability nodes. The time-lapse change in material constants for the high-porosity/permeability nodes are comparable with the background spatial fluctuations. Each of the points shown in Fig. 11 is therefore assumed to be a time-lapse scattering element with strength of the static fluctuation magnitude.

Fig. 12 illustrates the two parts of velocity seismogram simulation of backscattering and time-lapse signals for the $1/f$-noise earth volume. An initial and a final source pulse are provided by autocorrelation wavelets of a downhole orbital vibrator wavelet modelled for empirical 100-fold swept-frequency correlation wavelets (SMSITES 2001). The two source wavelets differ slightly in mechanical signal generation, giving a 5-parts-per-10^4 source-pulse difference. The initial and final time-lapse whole-cube background velocity vector seismograms $\mathbf{v}_i^{PP}(t)$ are superposed in the left-hand column of Fig. 12. The right-hand column shows the time-lapse image noise as the dotted-trace difference between the two left-hand column seismograms, $\Delta\mathbf{v}_i^{PP}(t)$, and the time-lapse image signal $\mathbf{v}_i^{\mathrm{TL}}(t = 2\xi/\alpha)$ as the solid-trace seismic scattering wavelet of the localized time-lapse oil–water substitution event in Fig. 11.

The Fig. 12 velocity seismograms are plotted on a timescale corresponding to a 3-m grid-node spacing; the amplitude scale is arbitrary. The time-lapse signal shown to occur at two-way traveltime 200 ms thus models an oil–water substitution event at a range $t \approx 100$ ms or ≈ 300 m for wave speed $\alpha = 3$ m ms^{-1}. The event is distributed over a data-cube volume of some 20 model nodes, corresponding to 60 m in simulation space. The time-lapse scattering event occupies only a small fraction of the enclosing 60 m subcube. The physically plausible, spatially convolved distribution of oil–water substitution changes in a heterogeneous reservoir has an equivalent scattering volume of 20 m on a side. Fig. 12 represents an estimate of the lower limit of time-lapse event detectability for the assumed source–signal stability and a single sensor. A more stable source, or a more pronounced time-lapse material property contrast, would reduce the detection threshold for a single sensor.

Multiple-sensor data, illustrated in Fig. 15, can readily detect time-lapse signal pulses of the size simulated in Fig. 12. The time-lapse signal is relatively stationary in time and waveform across a sensor array, while the background scattering signal varies essentially randomly across the array.

Once a pulse is identified as originating at a time-lapse reservoir event, it is straightforward to back-project the polarized *P*-wave vector motion (provided the signal is sufficiently large). The back-projected azimuth combines with the signal traveltime to locate the oil–water substitution event in the reservoir.

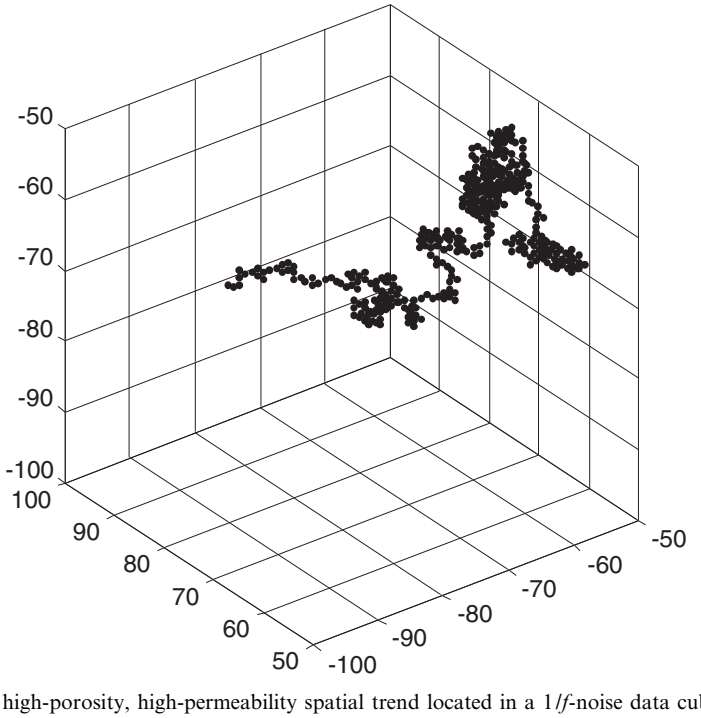

Figure 11. The configuration of a high-porosity, high-permeability spatial trend located in a $1/f$-noise data cube with 200 nodes on a side. Each plotted point represents a site for oil–water substitution during oil recovery, and therefore a site of time-lapse change in material constants that contributes a scattered wavelet to the time-lapse seismic imaging signal.

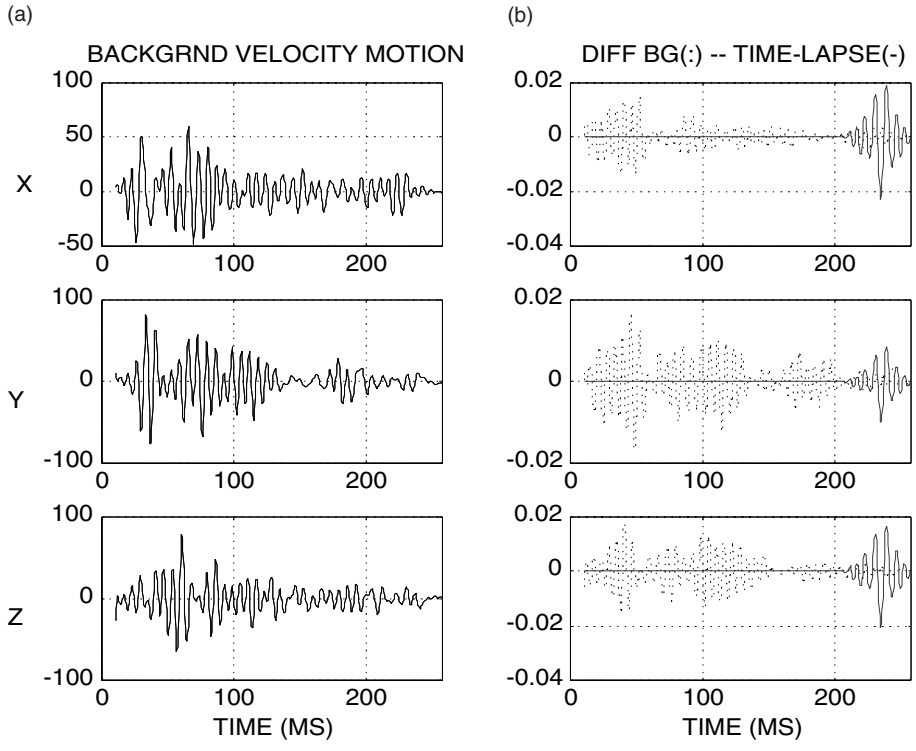

Figure 12. (a) Velocity vector seismograms of whole-cube scattering background. Seismograms for initial and final source wavelets are superposed but are indistinguishable at the level of plotting resolution. (b) Dashed trace shows the difference between the left-hand trace pairs; the solid trace shows the velocity vector scattering seismic motion from the high-permeability structure in Fig. 11. The recorded motion is the sum of the solid and dashed traces. As simulated, the time-lapse signal pulse cannot be easily distinguished from background noise for a single sensor, but the time-lapse signal can be readily distinguished in multisensor data.

4.2 Spatial location of time-lapse events

In addition to meeting the condition that the time-lapse signal can be detected against the static background residual as shown in Fig. 12, the time-lapse signal must be large enough relative to the residual imaging noise to locate the event in space. Fig. 13 shows a sample back-projection of a model signal *P*-waveform such as that of Fig. 12.

Provided the phase of the sensor components and the orientation of the horizontal sensors are known, and the coupling of the sensors to the borehole is uniform, *P*-wave motion back-projection will be accurate. Back-projection can be done graphically by estimating the magnitude of motion on each axis, say $[a, b, c]$, and forming the direction cosines $[\gamma_1, \gamma_2, \gamma_3] = [a, b, c]/(a^2+b^2+c^2)^{1/2}$, or by analytic means from the principal eigenvector of the vector-motion coherence matrix for the scattered wavelet signal. Let $u_i(t=n\Delta t)$, $i=1, 2, 3$, represent the time-lapse scattered signal + noise vector motion about a zero mean in the time interval $t_1 \le n\Delta t \le t_2$. Then the coherence matrix $\chi_{ij} = \Sigma_n\, u_i(n\Delta t)u_j(n\Delta t)$ represents how the vector motion is distributed about the three axes of motion. If all or the majority of motion is on a single axis, say $i=1$, the matrix element $\chi_{11} = u_1(n\Delta t)u_1(n\Delta t)$ will be large, and the remaining elements such as $\chi_{22} = u_2(n\Delta t)u_2(n\Delta t)$ and $\chi_{33} = u_3(n\Delta t)u_3(n\Delta t)$ will be small. Finding the orthogonal coordinate system that maximizes vector motion along one coordinate axis is the eigenvector problem for matrix χ_{ij}. Provided the coherent scattering signal from a localized oil–water substitution event is sufficiently large over incoherent background seismic noise, the determination of the principal eigenvector is robust.

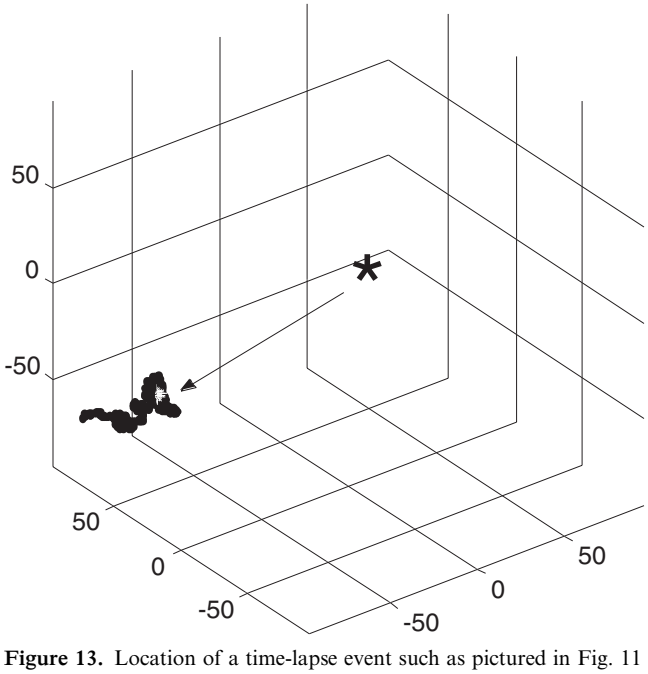

Figure 13. Location of a time-lapse event such as pictured in Fig. 11 using coherence-matrix analysis of time-lapse signal vector motion such as recorded in Fig. 12. The asterisk marks the centre of the data cube; the irregular black shape represents the oil–water interchange volume. The arrow points from the source to the white cavity in the oil–water interchange volume, denoting the location inferred from seismogram inversion.

Both the graphical and coherence matrix methods should be used to locate the scattering event. The coherence matrix method makes use of the entire information content of the wavelet, whereas the graphical method uses only a single, albeit the most important, bit of information. However, the graphical method is directionally unambiguous whereas the eigenvectors of the coherence matrix are subject to phase ambiguity that is often tricky to sort out. In the simulation example of Figs 11 and 12, the mean location of the oil–water substitution event is at data-cube node location [−49, 79, −66]. If the traveltime or radial variable is precisely known, the eigenvector inversion returns [−55, 77, −69], and the graphical method returns [−50, 80, −70].

4.3 Absolute amplitude of time-lapse seismic events

The third condition for detecting a time-lapse signal is that the signal be larger than the ambient seismic background and recording system noise. Considerable evidence indicates that borehole conditions can be sufficiently quiet that seismic background noise is smaller than the $\sim 0.1\mu$V rms amplifier/digitization noise typical of digital recording systems (e.g. Leary & Abercrombie 1994a,b; SMSITES 2001). The basic seismic signal record simulated in Fig. 12 has, then, to meet or exceed the $\sim 0.1\mu$V rms amplifier/digitization noise threshold of the recording system.

The amplitude of point-force scattering motion depends on the magnitude of the material property fluctuations ρ', λ', μ', on the summation of the random distribution of fluctuations over the successive scattering envelopes, and on the amplitude of the source pulse. Fig. 14 shows the absolute vector displacement motion computed from the fluctuating second-order radial derivative summand of (9c) weighted by radial offset geometric factor ξ^{-2}, $u^{PP}(t) \approx |\Sigma_{ijk}\{\xi^{-2}\partial_\xi^2(\alpha'/\alpha)\}_{ijk}\mathbf{e}_{ijk}|$ for a $1/f$-noise spatial distribution of random fluctuations with unit mean fluctuation amplitude.

The numerical amplitude t_0/t, $t_0 \approx 0.75$, of the displacement motion in Fig. 14 translates into an absolute amplitude for physical displacement motion when scaled by constants specifying the source amplitude and dimension u_0 and s_0, the scatterer mean fluctuation $\langle\alpha'/\alpha\rangle$, the unit size of the discretization $\Delta\xi$, and the angular aperture normalization factor $1/4\pi$.

A suite of near-field and far-field seismic data is available to characterize the physical displacement and effective dimension of the swept-frequency downhole orbital vibrator (DOV) borehole seismic source (SMSITES 2001). The orbital vibrator functions as a rotating point force in the borehole fluid acoustic medium. A DOV sweep signal is generated for 5–15 s over rotational frequencies from ~ 50 to ~ 300 Hz. An impulse-like correlation wavelet is formed by cross-correlating the DOV monitor signal with the far-field sensor signal.

Observation of the DOV near-field and far-field signals has yielded the following quantitative profile of the DOV borehole source radiation (SMSITES 2001). The source occupies a large percentage of the borehole column. A point-force acoustic wave excited by source displacement is effectively a plane wave in the subcentimetre annulus between the DOV and the borehole wall. The resulting far-field seismic radiation is accurately given by plane-wave acoustic diffraction at a slit of DOV height $h \approx 1$ m and borehole width $w \approx 0.1$ m. At distance ξ, the seismic diffraction field of the acoustic-to-seismic converted waves of length λ and source amplitude u_0 has magnitude $u(r) \approx u_0(w/\lambda)(h/\xi)$. The effective source dimension at frequency 200 Hz is then $s_0 = (wh/\lambda) \approx (0.1\text{ m})(1\text{ m})/(20\text{ m}) \approx (1/2)10^{-2}$ m. The DOV monitor geophone signal has peak voltage ≈ 150 mV

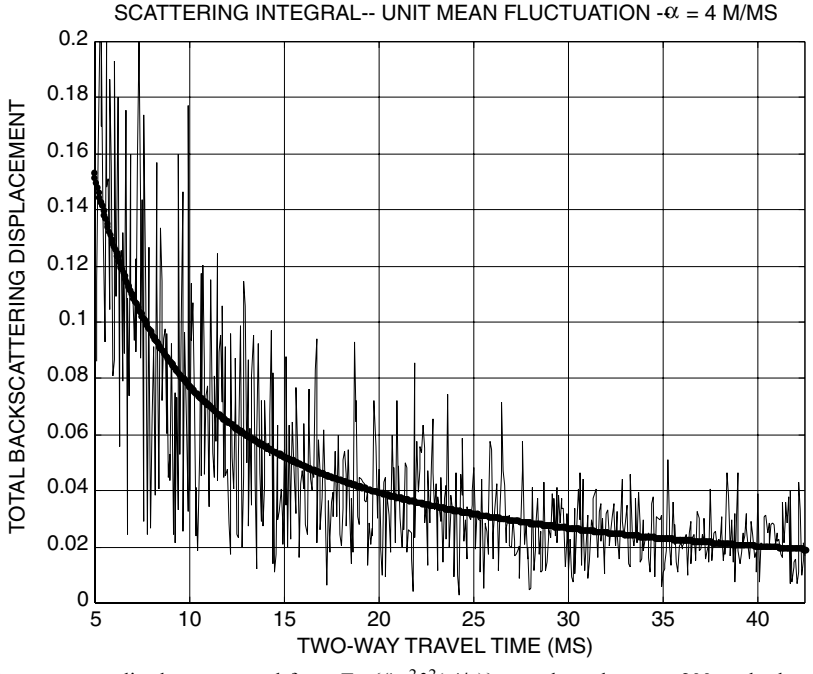

Figure 14. Calibration displacement amplitudes computed from $\Sigma_{ijk}\{\xi^{-2}\partial_\xi^2(\alpha'/\alpha)\}_{ijk}$ evaluated over a 200-node data cube with $1/f$-noise random fluctuations with unit rms fluctuation amplitude in elastic properties. The largest two-way traveltime within the data cube is ~ 45 ms at ~ 100 m radius scattering envelope in a medium of wave speed $\alpha = 4$ m ms^{-1}. The solid calibration curve is t_0/t, $t_0 \approx 0.75$. Scattering amplitude decay $\propto 1/$time is observed in coda waves (Leary & Abercrombie 1994a,b).

at 200 Hz, equivalent to a source displacement in the borehole fluid $u_0 \approx 10^{-5}$ m at 200 Hz. Plane wave acoustic-to-seismic conversion at the borehole fluid–solid interface introduces a factor $\approx 2/3$ for normal-incidence transmission, giving an effective source displacement $u_0 \approx 7 \times 10^{-6}$ m.

Using amplitude $\langle \alpha'/\alpha \rangle \approx 3$ per cent estimated from borehole logs, the backscatter displacement amplitude constant for use with the Fig. 14 calibration curve is $u_0 s_0 \Delta\xi \langle \alpha'/\alpha \rangle / 4\pi \approx 10^{-10}$ m^3 for $\Delta\xi = 1$ m. Multiplying this value by 0.02 m^{-2} from Fig. 14 for a 45 ms two-way traveltime gives $|\mathbf{u}_i^{PP}| \approx 2 \times 10^{-12}$ m for a scatterer offset $\xi \approx 100$ m and source frequency 200 Hz. The voltage excited by a single DOV frequency sweep in a sensor of transducer constant 15 V(m/s)$^{-1}$ by 2×10^{-12} m displacement at 200 Hz is $V \approx (4\pi)(200\ \mathrm{s}^{-1})(15\ \mathrm{V\ m}^{-1}\ \mathrm{s})(10^{-12}\ \mathrm{m}) \approx 4 \times 10^{-8}$ V $= 0.04$ μV, corresponding to the least significant bit of 24 bit signal digitization.

Signal correlation boosts the raw signal by a factor ≈ 30 to 1 μV. Stacking 1000 DOV sweeps (3 hr at 10 s/sweep) increases the signal-to-noise ratio by an additional factor of 30 relative to the uncorrelated background noise, yielding an effective 30 μV scattering signal relative to a 0.1 μV background noise level. If a back-scattering wavefield with 30 μV amplitude has the stability to resolve signals at the 0.1 μV level, a fluid-substitution event volume subtending 0.3 per cent of the total scattering area registers a signal at the signal-to-noise ratio ≈ 1 level of detection over ambient seismic/instrument noise. Expressing the solid angle fraction $d\Omega/4\pi \approx (1/2) \sin\theta d\theta \approx$ 0.5 per cent of 4π steradians in terms of the polar angle aperture $\Delta\theta$ gives $(1/2)\Delta\theta^2 \approx 2$(0.3 per cent), or $\Delta\theta \approx 0.1$. At $\xi \approx 100$ m offset, a scattering volume of angular aperture $\Delta\theta \approx 0.1$ has characteristic dimension $d \approx 2\xi\Delta\theta \approx 20$ m.

DOV wavelet signal and noise levels are illustrated by the cross-well data shown in Fig. 15. The upper panel shows the means of two DOV 750-sweep far-field correlation wavelets. The direct wavelet has traveled 300 m and arrives at the sensor with 5 μV amplitude. Following the direct wavelet for 30 ms to 60 ms, backscattering decays approximately as 1/time to 1 μV residual level. The $1/t$ time decay of the direct wavelet agrees with the scattering simulation of Fig. 14. The persistent 1 μV background scattering level is probably due to the highly layered Iceland basalts.

The lower panel calibrates the upper panel signal against two noise sources. The dashed line is the irreducible uncorrelated seismic background noise and recorder noise for a stack of 750 sweeps shown enhanced by a factor of 10. The solid line is the difference between the means of the two stacked signals of the upper panel. The irreducible background noise is ≈ 0.4 per cent of the direct wavelet and ≈ 1.5 per cent of the $1/t$-decay tail. The rms difference between the two direct wavelets is 4 per cent of the direct wavelet rms amplitude and 15 per cent of the $1/t$-decay tail. The signal stability level of Fig. 15 is due to numerical correlation noise affecting small signal amplitudes. At 100 m source–sensor offsets corresponding to modelled seismic backscatter signals, the observed far-field DOV signal would be 15 μV, comparable to the 30 μV simulation signal amplitude. More powerful DOV sources can produce signals up to 10 times larger than those recorded in Fig. 15, raising the scattering effective signal to 150–300 μV levels. At these larger signal levels, the correlation noise of Fig. 15 reduces to 0.1 per cent of the DOV signal level, thus giving field source signals approaching the observed DOV near-field source stability of a few parts in 10^4.

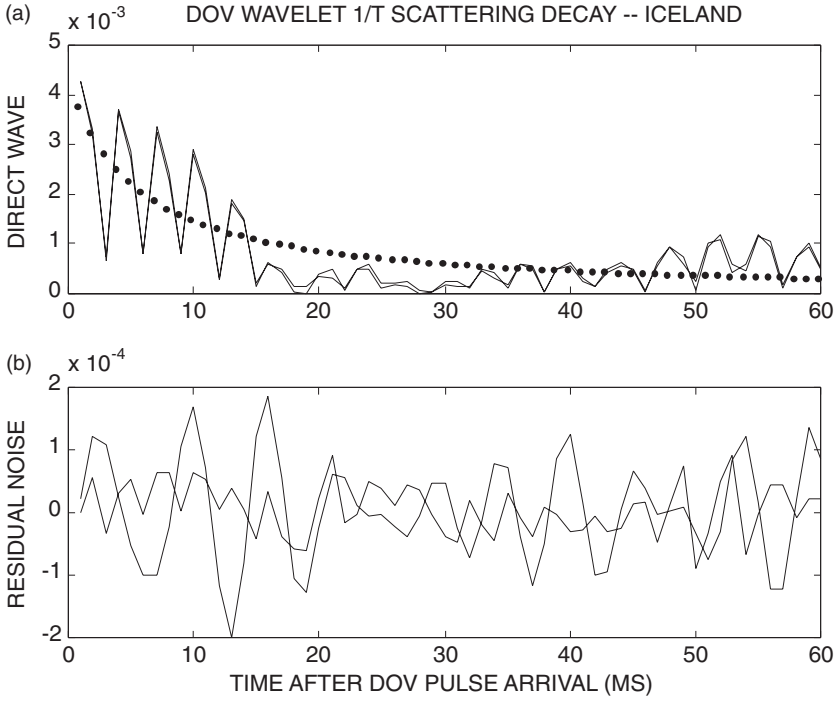

Figure 15. (a) Superposition of two DOV cross-well seismograms recorded with source and sensor at 500 m depth at 300 m separation. The direct arrival DOV wavelets decay inversely with time as in Fig. 14 synthetic backscattering wavelet. (b) Two types of seismic noise: (solid) difference between two mean wavelets shown in the top panel; (dashed) uncorrelated background noise gained by factor 10. Data are courtesy of SMSITES Project in Iceland (SMSITES 2001).

5 SPATIALLY CORRELATED STATIC STRUCTURES IN MULTISENSOR ARRAY DATA

A powerful diagnostic tool of exploration seismology is the identification of coherent scattering phases across seismograms from regularly spaced sensors. Borehole sensor arrays comprising 12 to 96 three-component geophones at intervals of 1–10 m are currently available to supply multisensor data for phase imaging time-lapse events such as oil–water substitution or for imaging static structures. It is therefore useful to apply the model scattering formalism to simulation of sensor data away from the origin. Formally this can be done by executing the frequency and radial variable integrals (6) and (7) for the source-wave argument $[i\omega(t-\xi/\alpha-|\boldsymbol{\xi}-\mathbf{r}|/\alpha)]$.

Multiple-sensor offsets can be finite but small compared with the scatterer offset. Then the source-wave argument expands to

$$[i\omega(t-2\xi/\alpha+\mathbf{r}\cdot\xi/\xi/\alpha)]=[i\omega(t-2\xi/\alpha+\cos\psi r/\alpha)]\,,$$

where ψ is the angle between the sensor offset $\mathbf{r}$ and the source plane wave propagation 1-axis. While in principle P–S and S–P converted waves are excited when $\mathbf{r}\cdot\boldsymbol{\xi}\neq 0$ and the sensor ray-path direction $\gamma_k\neq[1,\ 0,\ 0]$, in practice where $\xi\gg r$ converted waves are too small to register as independent components of a scattering seismogram. A wide-aperture array requires the more complex algebra given in Appendix C, where the δ-functions are expressed not in terms of a linear expression in the scatterer offset variable ξ, but in terms of the non-linear function $f(\xi)=t-\xi/\alpha-|\boldsymbol{\xi}-\mathbf{r}|/\alpha$.

For a general plane wave phase dependence of radial offset $\exp[i\omega f(\xi)]$, the infinite-frequency integrals are related to a δ-function that is zero everywhere except at the radial position ξ for which $f(\xi)=0$. The relevant general expressions are

$$\int d\omega\exp[i\omega f(\xi)]=\delta(f(\xi))\,, \tag{12a}$$

$$\int d\omega i\omega\exp[i\omega f(\xi)]=\int d\omega\partial_f\exp[i\omega f(\xi)]$$
$$=\partial_f\int d\omega\exp[i\omega f(\xi)]=\partial_f\delta(f(\xi))\,, \tag{12b}$$

$$\int d\omega\omega^2\exp[i\omega f(\xi)]=-\int d\omega\partial_f^2\exp[i\omega f(\xi)]$$
$$=-\partial_f^2\int d\omega\exp[i\omega f(\xi)]=-\partial_f^2\delta(f(\xi))\,. \tag{12c}$$

For small but finite sensor offsets,

$$f(\xi)=t+\cos\psi r/\alpha-2\xi/\alpha=t'-2\xi/\alpha\,,$$

and the phase effect alters the total traveltime from $t=2\xi/\alpha$ to $t=2\xi/\alpha-\cos\psi r/\alpha$. The spatial integrals (8) for P–P and S–S scattering appear with the geometric denominator $[\xi^2(1-r/\xi\ \cos\psi)]^{-1}\approx\xi^{-2}(1+r/\xi\ \cos\psi)$, inducing additional algebraic terms. Letting $M(\xi,\ \theta,\ \phi)$ and $M'(\xi,\ \theta,\ \phi)=\partial_\xi M(\xi,\ \theta,\ \phi)$ stand for the material property and spatial derivative for scattering point-force terms (2), the radial integrals for small but finite offset sensors become

$$\int\xi^2 d\xi d\cos\theta d\phi M'(\xi,\ \theta,\ \phi)[\xi^2(1-r/\xi\cos\psi)]^{-1}\partial_\xi\delta(t'-2\xi/\alpha)\,, \tag{13a}$$

$$\int\xi^2 d\xi d\cos\theta d\phi M(\xi,\ \theta,\ \phi)[\xi^2(1-r/\xi\cos\psi)]^{-1}\partial_\xi^2\delta(t'-2\xi/\alpha)\,. \tag{13b}$$

Cancelling the radial factors ξ^2 and ξ^{-2} and converting the δ-function derivatives to the derivatives of the material property and geometry terms gives

$$I_1(t)=\int d\xi\partial_\xi[M'(\xi,\ \theta,\ \phi)(1+r/\xi\cos\psi)]\delta(t'-2\xi/\alpha)\,, \tag{14a}$$

$$I_2(t)=\int d\xi\partial_\xi^2[M(\xi,\ \theta,\ \phi)(1+r/\xi\cos\psi)]\delta(t'-2\xi/\alpha)\,, \tag{14b}$$

Executing the first derivative gives

$$\partial_\xi[M'(\xi,\ \theta,\ \phi)(1+r/\xi\cos\psi)]$$
$$=\partial_\xi M'(\xi,\ \theta,\ \phi)+r/\xi\cos\psi\partial_\xi M'(\xi,\ \theta,\ \phi)$$
$$-r/\xi^2\cos\psi M'(\xi,\ \theta,\ \phi)\,, \tag{15a}$$

of which the first term corresponds to the sensor at the origin, the last is negligible, and the second represents a first-order correction to the first term due to finite sensor offset. The second spatial derivative gives

$$\partial_\xi^2[M(\xi,\ \theta,\ \phi)(1+r/\xi\cos\psi)]$$
$$=\partial_\xi^2 M(\xi,\ \theta,\ \phi)+r/\xi\cos\psi\partial_\xi^2 M(\xi,\ \theta,\ \phi)$$
$$-r/\xi^2\cos\psi\partial_\xi M(\xi,\ \theta,\ \phi)+\ldots\,. \tag{15b}$$

again retaining only the first and second terms. The radial integrals give

$$I_1(t)=\partial_\xi M'(\xi,\ \theta,\ \phi)|_{\xi=(\alpha t-r\cos\psi)/2}[1+2r\cos\psi/(\alpha t-r\cos\psi)]\,, \tag{16a}$$

$$I_2(t)=\partial_\xi^2 M(\xi,\ \theta,\ \phi)|_{\xi=(\alpha t-r\cos\psi)/2}[1+2r\cos\psi/(\alpha t-r\cos\psi)]\,. \tag{16b}$$

These expressions reduce to the existing scattering expression (9a) for $r=0$ and are stable for times $t\gg r/\alpha$, a condition equivalent to $r\ll\xi$. Numerical summation over the angular variables thus alters the summation over (9c) by the spherical amplitude term $2r\cos\psi/(\alpha t-r\cos\psi)$ and by the shift in plane wave traveltime $2r/\alpha\cos\psi$.

Fig. 16 illustrates the enhanced wavelet interpretation yielded by narrow-aperture multisensor time-lapse data. The time-lapse simulation of Fig. 12 is repeated for multiple sensors. The time-lapse signal visible in the single-sensor simulation of Fig. 12 is highly re-enforced in the multisensor data for Fig. 16. Seismogram fluctuations that could not be readily understood as signal or noise can now be assigned to the proper category. The signal moveout and amplitude systematics across the sensor array independently indicate that the oil–water substitution event is in line with, and is below, the sensor array. If the single-sensor data of Fig. 12 were more obscure, the multisensor data of Fig. 16 could be expected to detect the time-lapse signal wavelet.

A more difficult signal-identification task is finding a coherent signal in the backscattering image of a static scattering surface. With a very large number of sensors, it may be possible to discern a static vertical reflector such as a salt flank from a borehole embedded in rock adjacent to the salt dome. A more tractable scattering surface signal-identification problem occurs when the borehole is within the salt dome. Since salt is plastic over geological time, the elastic heterogeneities locked into the brittle fracture structure of rock are greatly reduced in

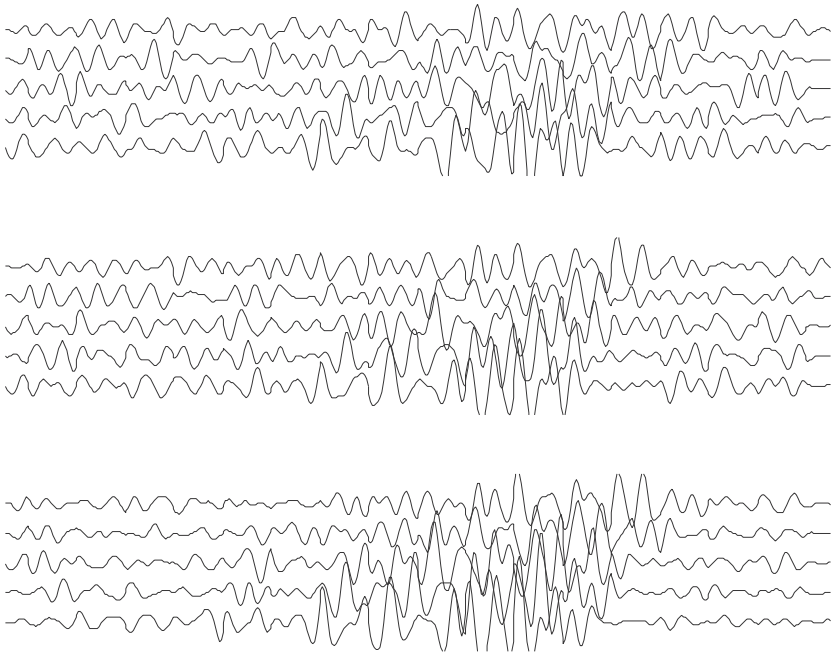

Figure 16. (Top to bottom) Suites of time-lapse-differenced [X, Y, Z]-component velocity seismograms for five sensors arrayed vertically through the source point. The time-lapse volume is that of Fig. 11; the centre trace of each array is that given in Fig. 12. Sensor offsets from the source are ± 3 and ± 6 data-cube nodes $\Delta\xi$. Multiple sensors give a clear indication of a coherent residual in the time-lapse difference data. The signal moveout confirms that the time-lapse scattering volume is in-line with the sensor array. The signal amplitude trend confirms that the scattering volume is below the array.

salt. A subvertical rock-salt reflecting surface may therefore be identifiable from within a salt dome if enough sensors are deployed.

To obtain a wide-angle sensor spread, the small-offset sensor constraint on the simulation of Fig. 16 is lifted, and the scattering amplitude expressions of Appendix C are used to compute the synthetic seismograms. Fig. 17 shows a sample result for an 11-sensor vertical borehole sensor spread about a centrally located borehole source.

A vertical reflecting wall is scaled to be located at a 180 m horizontal offset from a source embedded in a scattering volume scaled to be 400 m on a side. A suite of background

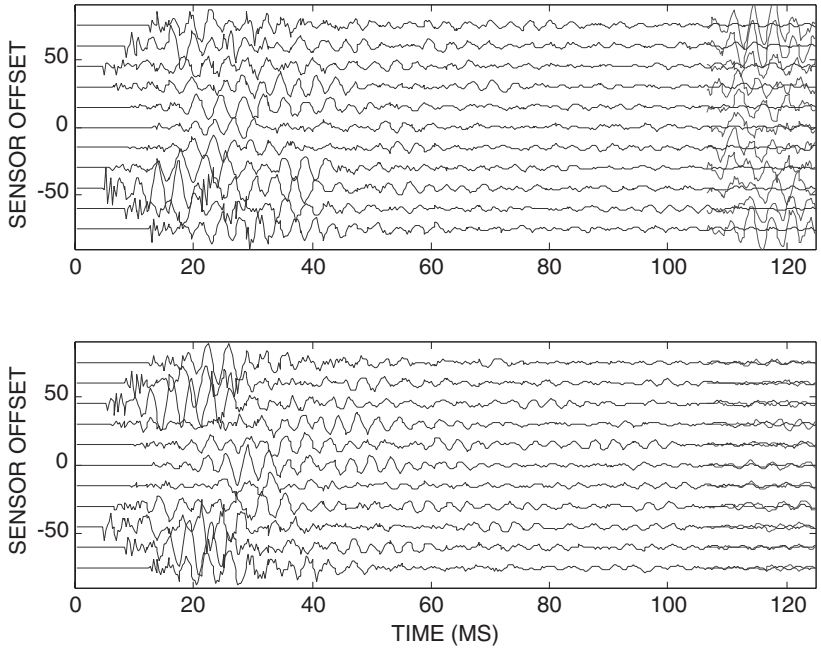

Figure 17. Simulation of a single-well scattering image of a vertical interface. The source is located in the centre of a vertical string of 11 sensors. Upper (lower) panel shows in-line (cross-line) horizontal motion of wide-aperture backscattered P waves. Backscatters from the vertical wall are small superposed arrivals at ~ 105 ms, with trace amplitudes increased by factor 25 for visibility.

scattering seismograms and reflected signal velocity seismograms are shown for the X (top) and Y (bottom) components of horizontal motion. The seismograms have frequencies ranging from 50 to 300 Hz. The reflected signal is computed for the same level of velocity contrast as the background velocity fluctuations, and is boosted by a factor of 25 in order to be visible against the seismic scattering background.

The $\times 25$ amplitude boost used in Fig. 17 to reveal the small backscattering signal from a distant planar static reflector indicates the difficulty of the task of identifying a coherent static structure in wide-aperture scattering in a $1/f$-noise medium. In a realistic scenario for which a vertical interface is not a smooth surface returning a coherent compact wavelet, signal identification might require a stacking fold of $25^2 \approx 600$. This might be achieved with an array of 25 sensors and 25 sources. If the velocity contrast is that of a rock–salt interface, the reflected wavelets would be perhaps three times larger, implying a stacking fold of $\sim$50–100, requiring 8–10 sensors and 8–10 sources for identification. If the source and sensors were inside the salt body, the background scattering due to salt-body elastic property fluctuations would be greatly reduced, and the signal reflected from the salt–rock interface might be seen with 10 sensors and a single source as the semi-coherent anomalous in-line motion arrivals of Fig. 17 (top).

The computation shown in Fig. 17 brings out an important aspect of a realistic scattering simulation for wide-aperture source–sensor geometry. For the wide-aperture scattering simulated in Fig. 17, in contrast with the narrow-aperture scattering simulated in Fig. 16, the reflected wavelet is not necessarily coherent across the sensor array. Trace stacking is not therefore as efficient in building a signal, as often assumed in surface seismics where the interfaces are presumed smooth, the reflected wavelets of coherent phase, and the background alone is uncorrelated random noise. In the simulation of Fig. 17, the desired signal is not effectively enhanced by summing the 11 sensor traces.

6 SUMMARY AND CONCLUSIONS

P-wave backscatter 'snapshots' of a heterogeneous rock volume can be acquired with a borehole seismic source and sensor located at the centre of the volume. Each scattering element (i, j, k) with characteristic dimension $\Delta\xi$ contributes backscatter motion in a radial direction $\mathbf{e}_{ijk}$ with amplitude given by the dimensionless second-order radial derivative $D^2_{ijk} = [\partial^2_\xi(\alpha'/\alpha)]_{ijk}\Delta^2\xi$ of local elastic property fluctuation $(\alpha'/\alpha)_{ijk}$. Backscattered P-wave motion at time $t = 2n\Delta\xi/\alpha$ and radial offset $\xi = n\Delta\xi$ is proportional to the areal sum controlled by the radial index constraint $n = (i^2 + j^2 + k^2)^{1/2}$:

$$\mathbf{A}(t = 2n\Delta\xi/\alpha) = \Sigma_{ijk}\Delta^2_{ijk}\mathbf{e}_{ijk}\,. \tag{17}$$

The total P-wave backscatter vector displacement $\mathbf{u}^{PP}(t)$ scales with source displacement u_0 and with the geometric scaling of the effective source dimension, s_0/ξ, and scatterer dimension, $\Delta\xi/\xi$, normalized to 4π steradians of solid angle:

$$\mathbf{u}^{pp}(t) \approx (1/4\pi)u_0(s_0/\xi)(\Delta\xi/\xi)\mathbf{A}(t)\,. \tag{18}$$

The overall scattering amplitude is a trade-off, $|\mathbf{A}(t)|/\xi^2$, between the combined spherical divergence $1/\xi^2$ of the source and scattered waves, and the sum $|\mathbf{A}(t)|$ over the increasing number of random fluctuation scattering volumes encountered by the expanding source wave. Numerical calibration (Fig. 14) of the areal summation (17) for unit rms fluctuation amplitude shows that the trade-off decays inversely with traveltime, $|\mathbf{A}(t)|/\xi^2 \approx t_0/t$, for $t_0 \approx 0.75$ ms m^2 for t in ms.

For traveltime t in ms and displacement in units of source displacement u_0, the Fig. 14 calibration curve t_0/t, gives the background P-wave scattering amplitude

$$u^{PP}(t) = |\mathbf{u}^{PP}(t) \approx (1/4\pi)u_0 s_0(t_0/t)\langle\alpha'/\alpha\rangle\,, \tag{19}$$

as scaled to a medium of rms fluctuation amplitude $\langle\alpha'/\alpha\rangle$ with unit scatterer size $\Delta\xi = 1$ m and mean P-wave velocity $\alpha = 4$ m ms^{-1}.

A repeat observation of (19) with slightly different experimental conditions is approximated by

$$u^{PP'}(t) \approx (1/4\pi)[u_0 s_0 + u_0\Delta s_0 + \Delta u_0 s_0]t_0/t \times [\langle\alpha'/\alpha\rangle + (\Omega/4\pi)\langle\alpha'/\alpha\rangle^{\mathrm{TL}}\delta(t-\tau)]\,, \tag{19'}$$

where $u_0\Delta s_0 + \Delta u_0 s_0$ expresses source instability, and $(\Omega/4\pi)\langle\alpha'/\alpha\rangle^{\mathrm{TL}}\delta(t-\tau)]$ expresses a time-lapse change in a crustal volume of aperture $(\Omega/4\pi)$ and material property change $\langle\alpha'/\alpha\rangle^{\mathrm{TL}}$ at radial offset given by two-way traveltime τ. The time-lapse difference between (19) and (19′),

$$u^{\mathrm{TL}}(t) = u^{PP'}(t) - u^{PP}(t) = u^0(t)[(\Omega/4\pi)\langle\alpha'/\alpha\rangle^{\mathrm{TL}}/\langle\alpha/\alpha\rangle - (\Delta s_0/s_0 + \Delta u_0/u_0)]\,, \tag{20}$$

gives concise, physically accurate expression to the conditions for time-lapse signal detection in terms of observable earth and experimental parameters:

$$|(\Omega/4\pi)\langle\alpha'/\alpha\rangle^{\mathrm{TL}}/\langle\alpha'/\alpha\rangle| \gtrsim |\Delta s_0/s_0| + |\Delta u_0/u_0|\,,$$

$$|u^{\mathrm{TL}}(t)| = u^0(t)[(\Omega/4\pi)\langle\alpha'/\alpha\rangle^{\mathrm{TL}}\delta(t-\tau)] \gtrsim |u^{\mathrm{MIN}}(t)|\,.$$

To be detected over experimental noise, the time-lapse scattering volume $\Omega/4\pi$ and the percentage physical change $\langle\alpha'/\alpha\rangle^{\mathrm{TL}}/\langle\alpha'/\alpha\rangle$ have to combine to exceed the background noise induced by fractional source instabilities $\Delta s_0/s_0$ and $\Delta u_0/u_0$, and the time-lapse signal $|u^{\mathrm{TL}}(t)|$ must exceed the minimum detectable signal $|u^{\mathrm{MIN}}(t)|$.

6.1 Time-lapse seismic imaging of fluid substitution events

Modelling indicates that signal wave amplitudes as in Fig. 12 can be achieved *in situ* with existing small-scale seismic equipment and practice for effective target fluid-substitution volumes of order 20 m on a side at distances of 100–200 m from the observation well. The modelling has essentially no adjustable physical parameters and is based on physical data rather than model assumptions.

(1) The permeability structures are associated with stochastic porosity distributions documented in Leary & Al-Kindy (2002).

(2) The time-lapse amplitude fluctuation associated with the changing fluid type in the permeability structure is fixed by laboratory observation at the amplitude of observed static fluctuations in elastic parameters (Wang & Nur 1992).

(3) The model vector motion is validated by (i) comparing the numerical sum over 4π steradians of solid back-scattering

angle with the closed mathematical expression for integration over a sphere; (ii) computing scattering seismogram temporal spectra for a wide range of spatial scaling distributions of random fluctuations; (iii) obtaining the $\sqrt{f}$ scattering seismogram temporal spectra observed in coda waves from scattering simulations for spatial fluctuations observed *in situ*; and (iv) observing $1/t$-temporal decay of cross-well records of direct arrivals.

(4) The absolute amplitude of time-lapse seismogram motion is computed from borehole source performance data using the DOV (downhole orbital vibrator). At currently available source power, the time-lapse signal of stacked, multisensor data is somewhat above the sensor detection threshold. The modelled time-lapse signal-to-noise threshold for a fluid-substitution volume of 20 m at 100–200 m offset, $S/N \approx (20\ m/2/100\ m)^2 \approx$ 0.25–1 per cent, is comparable to demonstrated levels of borehole source and sensor stability and borehole source radiation power. Increased source power and sensor sensitivity will, however, greatly increase the range of time-lapse event detection. A peak frequency of 1 kHz, a longer DOV, and increased displacement u_0 are feasible engineering steps that can boost DOV wavelet amplitude by a factor of 10–20 without sacrificing signal stability. Stacked sensors can boost sensitivities by a factor of 3–5. Modelling indicates that these source signal and sensor sensitivity boosts can increase the time-lapse event detection resolution to an aperture of 20 m at 300–500 m offsets.

6.2 Static event seismic imaging

Static event imaging in crustal rock seems a distant prospect, except, perhaps, in the unusual circumstances of a nearby coherent reflector and relatively low scattering background, as might be afforded by operations in the interior of a salt body. The need to build sufficient fold in an axial sensor array at high seismic frequencies in order to overcome volumetric background scattering noise appears to be beyond presently available source and sensor resources (e.g. Tura & Cambois 2001). If the scattering noise is substantially reduced by operating within a salt body rather than in the surrounding rock formations, it may be possible to obtain images of the static salt–rock interface from an axial source–sensor array. An important aspect of operating at high seismic frequencies is that reflection surfaces may not support the smooth-interface approximation used for signal stacking in low-frequency surface seismic imaging. If the static interface is rough, high-frequency scattered wavelets are not very coherent, undermining the stacking tactic that efficiently enhances low-frequency coherent planar interface reflected wavelets relative to uncorrelated random background wave motion.

6.3 Borehole seismic image modelling to guide future development

The principles of time-lapse borehole seismic imaging are straightforward. Successful implementation needs stable, adequately powerful seismic sources that, combined with a sufficient number of stable vector motion sensors in a single well, can produce seismic snapshots sufficiently deep into the reservoir to make their deployment a potentially cost-effective oilfield production tool. The physical model of reservoir heterogeneity and seismic scattering presented here appears to provide a reliable guide to time-lapse seismic imaging in order to consolidate present engineering capability, and to promote effective routes to increased capability in the near future.

ACKNOWLEDGMENTS

High-resolution borehole seismic imaging in heterogeneous media, particularly of oil–water substitution events in producing hydrocarbon reservoirs, has been a continuing joint interest with Stuart Crampin and Larry Walter. The University of Edinburgh-led Uniwell Project supported by Geospace Engineering Resources International (GERI), Amerada-Hess Ltd, Conoco UK Ltd, Exxon Research Corporation, Mobil North Sea Ltd, and the UK Department of Trade and Industry provided the impetus for significant developments by GERI to the orbital vibrator borehole seismic source used to model time-lapse seismic data noise figures. The EU-funded SMSITES Project held by Stuart Crampin has, with the co-operation of GERI, provided empirical data on achievable source stability essential to effective time-lapse seismometry. Mark Stephenson of Marathon Oil UK kindly supplied the well-core data needed to physically model the permeability structure of reservoir rock. Comments on the original manuscript from John Hudson, Ilya Tsvankin and Enru Liu improved the presentation.

REFERENCES

Aki, K. & Richards, P., 1980. *Quantitative Seismology, Theory and Methods,* W. H. Freeman & Co., San Francisco.

Al-Kindy, F., 1999. Broadband (cm to km) power-law scaaling heterogeneity in the Earth's crust: evidence from fractal analysis of geophysical borehole logs, *MSc thesis,* University of Edinburgh, Edinburgh.

Christie, P. & Ebrom, D., 2000. Development and production (Special Section), *Leading Edge,* **19,** 275–310.

Dubendorff, B. & Menke, W., 1986. Time-domain apparent-attenuation operators for compressional and shear waves: experiment versus single scattering theory, *J. geophys. Res.,* **91,** 14 023–14 032.

Dumont, M.-H., Fayemendy, C., Mari, J.-L. & Huguet, F., 2001. Underground gas storage: estimating gas column height and saturation with time lapse seismics, *Petrol. Geosci.,* **7,** 123–129.

Dunlop, K.N.B., King, G.A. & Breitnback, E.A., 1988. Monitoring of oil/water fronts by direct measurement, SPE no. 18271, *Soc. petrol. Eng. Ann. Mtg*.

Ebrom, D., Li, X. & Sukup, D., 2000. Facilitating technologies for permanently instrumented oil fields, *Leading Edge,* **19,** 282–285.

Francis, A. & Pennington, W., 2001. Development and production (Special Section), *Leading Edge,* **20,** 269–328.

Frankel, A. & Clayton, R.W., 1986. Finite difference simulations of seismic scattering: implications for the propagation of short-period seismic waves in the crust and models of crustal heterogeneity, *J. geophys. Res.,* **91,** 6465–6489.

Greaves, R.J. & Fulp, T.J., 1987. Three-dimensional seismic monitoring of an enhanced oil recovery process, *Geophysics,* **52,** 1175–1187.

Gutierrez, M.A., Dvorkin, J. & Nur, A., 2001. Thoeretical rock physics for bypassed oil detection behind the casing: La Cira-infantas oil field, *Leading Edge,* **20,** 192–197.

Hoshiba, M., 1991. Simulation of multiple-scattered coda wave excitation based on the energy conservation law, *Phys. Earth planet. Inter.,* **67,** 123–136.

Hudson, J.A., 1977. Scattering waves in the coda of *P*, *Geophys. J.,* **43,** 359–374.
Jack, I., 2001. The coming of age for 4D seismic, *First Break,* **19,** 24–45.
Justice, J.H., Vassiliou, A.A., Singh, S., Logel, J.D., Hansen, P.A., Hall, B.R., Hutt, P.R. & Solanki, J.J., 1992. Acoustic tomography for monitoring enhanced oil recovery, *Leading Edge,* **8,** 12–19.
Leary, P.C., 1991. Deep borehole log evidence for fractal distribution of fractures in crystalline rock, *Geophys. J. Int.,* **107,** 615–627.
Leary, P.C., 1995. The cause of frequency-dependent seismic absorption in crustal rock, *Geophys. J. Int.,* **122,** 143–151.
Leary, P.C., 1997. Rock as critical-point system and the inherent implausibility of reliable earthquake prediction, *Geophys. J. Int.,* **131,** 451–466.
Leary, P.C., 1998. Relating microscale rock-fluid interactions to macro-scale fluid flow structures, in *Faulting, Fault Sealing and Fluid Flow in Hydrocarbon Reservoirs, Geol. Soc. Lond. Spec. Publ.,* **147,** 242–269.
Leary, P.C. & Abercrombie, R.E., 1994a. Frequency dependent crustal scattering and absorption at 5–160 Hz from coda decay observed at 2.5 km depth, *Geophys. Res. Lett.,* **21,** 971–974.
Leary, P.C. & Abercrombie, R.E., 1994b. Fractal surface scattering origin of S-wave coda: spectral evidence from recordings at 2.5 km, *Geophys. Res. Lett.,* **21,** 1683–1686.
Leary, P.C. & Al-Kindy, F., 2002. Spatially correlated 1/f-noise porosity and log (permeability) sequences in well core, *Geophys. J. Int.,* this issue.
Li, X. & Hudson, J.A., 1997. Time-domain computation of scattering from a heterogeneous layer, *Geophys. J. Int.,* **128,** 197–203.
Mandelbrot, B.B., 1983. *The Fractal Geometry of Nature,* W.H. Freeman and Co., San Francisco.
Mandelbrot, B.B., 1999. *Multifractals and 1/f Noise,* Springer-Verlag, New York.
Martin, M.A. & Davis, T.L., 1987. Shear-wave birefringence: A new tool for evaluating fractured reservoirs, *Leading Edge,* **6,** 22–28.
Matlab, 2000. *High-Performance Numerical Compuation and Visualisation Software,* The Math Works Inc., info@mathworks.com
Matsunami, K., 1991. Laboratory tests of excitation and attenuation of coda waves using 2-D models of scattering media, *Phys. Earth planet. Inter.,* **67,** 36–47.
Mathews, L., 1992 3-D seismic monitoring of an in-situ thermal process: Athabasca Canada, in Reservoir Geophysics, *Investigations in Geophysics,* Vol. 7, pp. 301–308, ed. Sheriff, R.E., Soc. explor. Geophys., Tulsa.
Oil & Gas Industry Task Force, 2001. Bringing research and technology to optimise reservoir performance, *First Break,* **19,** 351–365.
Paulsson, B.N.P., Heredith, J.A., Wang, Z. & Fairborn, J.W., 1994. The Steepbank crosswell seismic project, Reservoir definition and evaluation of steamflood technology, *Leading Edge,* **13,** 737–747.
Pullen, N.E., Jackson, R.K., Matthews, L.W., Hirshe, W.K. & den Boer, L.D., 1987. 3-D imaging of heat zones in an athabasca tar sands thermal pilot, in *Soc. explor. Geophys. 54th Ann. Mtg Expanded Abstracts,* pp. 391–394.
Roth, M. & Korn, M., 1993. Single-scattering theory versus numerical modelling in 2-D random media, *Geophys. J. Int.,* **112,** 124–140.
Sheriff, R.E. (ed.), 1992. Reservoir Geophysics, *Investigations in Geophysics,* Vol. 7**,** Soc. explor. Geophys., Tulsa.
SMSITES, 2001. SMSITES Project Report UEDIN-s1-21, whttp://www.smsites.org
Sparkman, G., 1998. Time lapse or time elapse (Special Section), *Leading Edge,* **17,** 1386–1458.
Tura, A. & Cambois, G., 2001. Instrumented oil fields (Special Section), *Leading Edge,* **20,** 613–648.
Turcotte, D.L., 1992. *Fractals and Chaos in geology and Geophysics,* Cambridge University Press, Cambridge.
van Riel, P., 2000. The past, present and future of quantitative reservoir characterisation, *Leading Edge,* **19,** 878–881.
Wang, Z. & Nur, A., 1992. *Seismic and Acoustic Velocities in Reservoir Rocks,* Geophys. Reprint ser. 10, Soc. explor. Geophys., Tulsa.

APPENDIX A: LIST OF SYMBOLS AND THEIR SI UNITS

Properties of crustal rock

α, α', β, β': mean and spatially variable *P*- and *S*-wave velocities; $[\alpha, \alpha', \beta, \beta'] = \mathrm{m\ ms^{-1}}$.
ρ, ρ': mass density; $[\rho, \rho'] = \mathrm{kg\ m^{-3}}$.
λ, λ', μ, μ': mean and spatially variable Lamé elastic moduli; $[\lambda, \lambda', \mu, \mu'] = \mathrm{N\ m^{-2}} = (\mathrm{kg\ m^{-3}})(\mathrm{m\ s^{-2}})$.
B: power-law-scaling exponent for spatial fluctuations of elastic properties.

Properties of seismic source

ω: source frequency; $[\omega] = \mathrm{s^{-1}}$.
u_0: effective source displacement amplitude at source; $[u_0] = \mathrm{m}$.
s_0: effective source dimension; $[s_0] = \mathrm{m}$.
τ_0: unit time interval of seismograms; $[\tau_0] = \mathrm{ms}$.
DOV: downhole orbital vibrator borehole seismic source.
w: width of DOV borehole acoustic source.
h: height of DOV borehole acoustic source.
λ: wavelength of DOV borehole source peak radiation.
t_0: empirical normalization constant for 1/time decay of far-field wavelet.
$S^0(\omega)$: amplitude of source at frequency ω; $[S^0(\omega)] = [u_0 s_0 \tau_0] = \mathrm{m^2\ s}$.
u^P, u^S: magnitude of *P* and *S* source waves at scatterer; $[u^P, u^S] = \mathrm{m}$.
u^{PP}, u^{SS}: magnitude of *P*–*P* and *S*–*S* backscattered waves at sensor; $[u^{PP}, u^{SS}] = \mathrm{m}$.

Seismic displacement radiation field

$\mathbf{u}'(t)$, $u_i'(t)$: general scattered vector displacement wavefield; $[\mathbf{u}'(t), u_i'(t)] = \mathrm{m}$.
$\mathbf{r}$, r: vector location and scalar offset of sensor relative to source; $[\mathbf{r}, r] = \mathrm{m}$.
t: time; $[\mathrm{t}] = \mathrm{ms}$.
$\boldsymbol{\xi}$, $\xi = |\boldsymbol{\xi}|$: radius vector and scalar distance from source to scatterer; $[\xi] = \mathrm{m}$.
$\gamma_i \equiv \mathbf{e}_\xi$: direction cosine, unit vector of ray paths to/from source/sensor and scatterer; $[\gamma_i, \mathbf{e}_\xi] = 1$.
$\Im_i$: point force giving rise to displacement wavefield $u_i'(t)$; $[\Im_i] = \mathrm{N} = \mathrm{kg\ m\ s^{-2}}$.
θ: angle between source–scatterer direction and the 1-axis of the vector sensor.
δ_{ij}: Kronecker unit tensor; $[\delta_{ij}] = 1$.
F_k: secondary source effective point-force density of scattering heterogeneity; $[F_k] = \mathrm{N\ m^{-3}}$.
$\delta(x)$: Dirac delta function; $[\delta(x)] = [x^{-1}]$.

Numerical data cube and synthetic scattering seismograms

$\Delta\xi$: spatial discretization interval, $\mathrm{O}(\sim 1\ \mathrm{m})$; $[\Delta\xi] = \mathrm{m}$.
Δt: seismogram sample interval, $\mathrm{O}(\Delta \mathrm{t}) \sim 1\ \mathrm{ms}$; $[\Delta t] = \mathrm{s}$.
a: correlation scale-length of random medium for non-power-law-scaling media.
B: power-law-scaling exponent of data-cube spatial fluctuations.
A as exponent: power-law-scaling exponent of scattering seismogram temporal fluctuations.

D^2_{ijk}: second radial derivative of spatial elastic property fluctuations α'/α at data-cube node (i, j, k).
$\mathbf{A}(t)$: areal sum over dimensionless scattering amplitudes $D^2_{ijk}(\alpha'/\alpha)_{ijk}\Delta\xi^2$ for $n^2=(i^2+j^2+k^2)$.

APPENDIX B: NARROW APERTURE *P–P* AND *S–S* SCATTERING POINT FORCES

The point force of Aki & Richards (1980, Section 13.2.3) is evaluated in a coordinate system defined by the direction of the plane source wave. Scatterer location is denoted by radial distance ξ along the 1-axis. Point-force component F_1 is along the source direction, and point-force components F_2 and F_3 are orthogonal to the direction of plane-wave travel. The phase of the point force relative to the source is given by the plane travelling wave $\exp[i\omega(t-\xi/\alpha)]$ for P waves, and $\exp[i\omega(t-\xi/\beta)]$ for S waves. Partial differentiation along the k-axis is denoted ∂_k with $\partial_1=\partial_\xi$ denoting radial differentiation.

$$F_k = -\rho'\partial_t^2 u_k + (\lambda'+\mu')\partial_k(\partial_i u_i) + \mu'\partial_i\partial_i u_k + \partial_k\lambda'\partial_i\mu_i + \partial_i\mu'(\partial_i u_k + \partial_k u_i)\,, \tag{B1}$$

$$u_k^P(t|\xi,\omega) = S^0(\omega)\exp[i\omega(t-\xi/\alpha)][1,0,0] \tag{B2a}$$

$$u_k^S(t|\xi,\omega) = S^0(\omega)\exp[i\omega(t-\xi/\beta)][0,1,0]\,. \tag{B2b}$$

P wave

$$-\rho'\partial_t^2 u_k = -\rho^1[1,0,0]\partial_t^2 u_k = -\rho^1[-\omega^2,0,0]u\,,$$

$$(\lambda'+\mu')\partial_k(\partial_i u_i) = (\lambda'+\mu')[\partial_1,0,0]\partial_i u_i = (\lambda'+\mu')[\partial_1,0,0](\partial_1 u_1+0+0) = (\lambda'+\mu')[-\omega^2,0,0]u\,,$$

$$\mu'\partial_i\partial_i u_k = \mu'[\partial_1^2,0,0]u = \mu'[-\omega^2,0,0]u\,,$$

$$\partial_k\lambda'\partial_i u_i = [\partial_1\lambda',\partial_2\lambda',\partial_3\lambda'](\partial_1 u_1+0+0) = -i\omega/\alpha[\partial_1\lambda',\partial_2\lambda',\partial_3\lambda']u\,,$$

$$\partial_i\mu'\partial_i u_k = (\partial_1\mu'\partial_1+\partial_2\mu'\partial_2+\partial_3\mu'\partial_3)[u_1,0,0] = [\partial_1\mu'\partial_1 u,0,0] = \partial_1\mu'[-i\omega/\alpha,0,0]u\,,$$

$$\partial_i\mu'\partial_k u_i = [\partial_i\mu'\partial_1 u_i,\partial_i\mu'\partial_2 u_i,\partial_i\mu'\partial_3 u_i] = [\partial_1\mu'\partial_1 u_1+\partial_2\mu'\partial_1 u_2+\partial_3\mu'\partial_i u_3,\partial_1\mu'\partial_2 u_1+\partial_2\mu'\partial_2 u_2 + \partial_3\mu'\partial_2 u_3,\partial_1\mu'\partial_3 u_1+\partial_2\mu'\partial_3 u_2+\partial_3\mu'\partial_3 u_3] = [\partial_1\mu'\partial_1 u_1,0\;0] = \partial_1\mu'[-i\omega/\alpha,0\;0]u\,.$$

Hence

$$F_1^P = [+\rho^1\omega^2-\omega^2(\lambda'+2\mu')-i\omega/\alpha\partial_1(\lambda'+2\mu')]u^P\,,$$

$$F_2^P = -i\omega/\alpha\partial_2\lambda' u^P\,,$$

$$F_3^P = -i\omega/\alpha\partial_3\lambda' u^P\,,$$

which for backscattering contracts to

$$\gamma_i\gamma_k F_k^P = [1,0,0][F_1^P,F_2^P,F_3^P] = [1,0,0](\rho'\omega^2-\omega^2(\lambda'+2\mu')-i\omega/\alpha\partial_1(\lambda'+2\mu'))u^P\,. \tag{B3}$$

S wave

$$-\rho'\partial_t^2 u_k' = -\rho'[0,1,0]\partial_t^2 u_k' = -\rho'[0,-\omega^2,0]u\,,$$

$$(\lambda'+\mu')\partial_k(\partial_i u_i) = (\lambda'+\mu')[\partial_1,0,0]\partial_i u_i = (\lambda'+\mu')[\partial_1,0,0](\partial_1 u_1+0+0) = [0,0,0]\,,$$

$$\mu'\partial_i\partial_i u_k = \mu'[0,\partial_1^2,0]u' = \mu'[0,-\omega^2,0]u\,,$$

$$\partial_k\lambda'\partial_i u_i = [\partial_1\lambda',\partial_2\lambda',\partial_3\lambda'](\partial_1 u_1+0+0) = [0,0,0]\,,$$

$$\partial_i\mu'\partial_i u_k = (\partial_1\mu'\partial_1+\partial_2\mu'\partial_2+\partial_3\mu'\partial_3)[0,u_2,0] = [0,\partial_1\mu'\partial_1 u,0,0] = \partial_1\mu'[0,-i\omega/\alpha,0]u\,,$$

$$\partial_i\mu'\partial_k u_i = [\partial_i\mu'\partial_1 u_i,\partial_i\mu'\partial_2 u_i,\partial_i\mu'\partial_3 u_i] = [\partial_1\mu'\partial_1 u_1+\partial_2\mu'\partial_1 u_2+\partial_3\mu'\partial_1 u_3,\partial_1\mu'\partial_2 u_1+\partial_2\mu'\partial_2 u_2 + \partial_3\mu'\partial_2 u_3,\partial_1\mu'\partial_3 u_1+\partial_2\mu'\partial_3 u_2+\partial_3\mu'\partial_3 u_3] = [\partial_2\mu'\partial_1 u_2,0,0] = \partial_2\mu'[-i\omega/\alpha,0,0]u\,.$$

Hence

$$F_1^S = -i\omega/\alpha\partial_2\mu^1 u^S\,,$$

$$F_2^S = [+\rho'\omega^2-\omega^2\mu'-i\omega/\beta\partial_1\mu')]u^S\,,$$

$$F_3^S = 0\,,$$

which for backscattering contracts to

$$(\delta_{ik}-\gamma_i\gamma_k)F_k^S = [F_1^S,F_2^S,0]-(F_1^S\;0,0] = [0,F_2^S,0] = [0,1,0](\rho'\omega^2-\omega^2\mu'-i\omega/\alpha\partial_1\mu')u^S\,. \tag{B4}$$

APPENDIX C: SCATTERING AMPLITUDES FOR A GENERAL SENSOR OFFSET

Let the phase of the plane wave source function be $i\omega f(\xi)$, where $f(\xi)=t-\xi/\alpha-|\mathbf{r}-\boldsymbol{\xi}|/\alpha$. Assigning coordinates to the scatterer and sensor positions, $\boldsymbol{\xi}=[\xi,0,0]$ and $\mathbf{r}=[x,0,z]$,

$$f(\xi) = t-\xi/\alpha-[(\xi-x)^2+z^2]^{1/2}/\alpha = t-\xi/\alpha-(\xi^2-2x\xi+r^2)^{1/2}/\alpha\,.$$

For plane wave phase dependence on radial offset $\exp[i\omega f(\xi)]$, the infinite frequency integrals are related to a δ-function that is zero everywhere except at the radial position ξ for

which $f(\xi)=0$:

$$\int d\omega \exp[i\omega f(\xi)] = \delta(f(\xi)), \tag{C1}$$

$$\int d\omega i\omega \exp[i\omega f(\xi)] = \int d\omega \partial_f \exp[i\omega f(\xi)] = \partial_f \int d\omega \exp[i\omega f(\xi)] = \partial_f \delta(f(\xi)), \tag{C2}$$

$$\int d\omega \omega^2 \exp[i\omega f(\xi)] = -\int d\omega \partial_f^2 \exp[i\omega f(\xi)] = -\partial_f^2 \int d\omega \exp[i\omega f(\xi)] = -\partial_f^2 \delta(f(\xi)). \tag{C3}$$

Let $M(\xi, \theta, \phi)$ and $M'(\xi, \theta, \phi)=\partial_\xi M(\xi, \theta, \phi)$ stand for the material property spatial and spatial derivative dependence of scattering point-force terms. We wish to evaluate the radial integrals

$$I_1(t, \theta, \phi) = \int d\xi M'(\xi, \theta, \phi)\xi/[(\xi - x)^2 + z^2)]^{1/2} \partial_f \delta(f(\xi)),$$

$$I_2(t, \theta, \phi) = \int d\xi M(\xi, \theta, \phi)\xi/[(\xi - x)^2 + z^2)]^{1/2} \partial_f^2 \delta(f(\xi)).$$

From the definition of the function $f(\xi)$,

$$\xi = (1/2)[\alpha^2(t-f)^2 - r^2]/[\alpha(t-f) - x].$$

Since $\xi > 0$, both denominator

$$\alpha(t-f) - x = \xi + (\xi^2 - 2x\xi + x^2 + z^2)^{1/2} - x > 0$$

and numerator

$$\alpha^2(t-f)^2 - r^2 = [\xi + (\xi^2 - 2x\xi + r^2)^{1/2}]^2 - r^2 > 0$$

are positive-definite and ξ is everywhere finite. If the sensor is colocated with the source, x, $z \to 0$ and $\xi \to \alpha(t-f)/2$.

In order to perform the integration over the δ-function, the integration variable is changed from ξ to $f(\xi)$:

$$\begin{aligned} I_1(t, \theta, \phi) &= \int d\xi M'(\xi, \theta, \phi)\xi/[(\xi - x)^2 + z^2]^{1/2} \partial_f \delta(f) \\ &= \int df \partial_f \xi M'(\xi(f), \theta, \phi)\xi(f)/[(\xi(f) - x)^2 + z^2]^{1/2} \partial_f \delta(f) \\ &= -\int df \partial_f \{[\partial_f \xi] M'(\xi(f), \theta, \phi)\xi(f) \\ &\quad /[(\xi(f) - x)^2 + z^2)]^{1/2}\} \delta(f) \\ &= -\partial_f \{[\partial_f \xi] M'(\xi(f), \theta, \phi)\xi(f) \\ &\quad /[(\xi(f) - x)^2 + z^2)]^{1/2}\}|_{f=0}. \end{aligned}$$

Expressing terms of $I_1(t, \theta, \phi)$ as

$$\begin{aligned} \partial_f \xi &= (1/2)\partial_f [(\alpha^2(t-f)^2 - r^2)/(\alpha(t-f) - x)] \\ &= -\alpha^2(t-f)/[\alpha(t-f) - x] \\ &\quad - (1/2)[\alpha^2(t-f)^2 - r^2](-\alpha)/[\alpha(t-f) - x]^2 \\ &= -\alpha\{\alpha(t-f)[\alpha(t-f) - x] \\ &\quad - (1/2)[\alpha^2(t-f)^2 - r^2]\}/[\alpha(t-f) - x]^2 \\ &= -\alpha[(1/2)\alpha^2(t-f)^2 - \alpha(t-f)x \\ &\quad + (1/2)(x^2 + z^2)]/[\alpha(t-f) - x]^2 \\ &= -\alpha/2[\alpha^2(t-f)^2 - 2\alpha(t-f)x + x^2 + z^2]/[\alpha(t-f) - x]^2 \\ &= -\alpha/2[1 + z^2/(\alpha(t-f) - x)^2], \end{aligned}$$

Using algebraic expressions

$$\partial_f^2 \xi = -\alpha^2 z^2/[\alpha(t-f) - x]^3,$$

$$[(\xi - x)^2 + z^2]^{1/2} = \alpha(t-f) - \xi,$$

$$\xi/[(\xi - x)^2 + z^2]^{1/2} = \xi/[\alpha(t-f) - \xi],$$

and

$$\partial_f \{\xi/[(\xi - x)^2 + z^2]^{1/2}\} = \alpha[\xi + (t-f)\partial_f \xi]/[\alpha(t-f) - \xi]^2,$$

the first integral becomes

$$\begin{aligned} I_1(t, \theta, \phi) &= -\partial_f \{[\partial_f \xi] M'(\xi(f), \theta, \phi)\xi(f) \\ &\quad /[(\xi(f) - x)^2 + z^2)]^{1/2}\}|_{f=0} \\ &= -\{\partial_f^2 \xi\, M'(\xi(f), \theta, \phi)\xi(f) \\ &\quad /[(\xi(f) - x)^2 + z]^{1/2}\}|_{f=0} \\ &\quad - \{\partial_f \xi\, \partial_f M'(\xi(f), \theta, \phi)\xi(f) \\ &\quad /[(\xi(f) - x)^2 + z^2]^{1/2}\}|_{f=0} \\ &\quad - \{\partial_f \xi M'(\xi(f), \theta, \phi)\partial_f [\xi(f) \\ &\quad /[(\xi(f) - x)^2 + z^2]^{1/2}]\}|_{f=0} \\ &= \{\alpha^2 z^2/[\alpha(t-f) - x]^3 M'(\xi(f), \theta, \phi) \\ &\quad \xi/[\alpha(t-f) - \xi]^{1/2}\}|_{f=0} \\ &\quad + (\alpha/2)[1 + z^2/(\alpha(t-f) - x)^2]\partial_\xi M'(\xi(f), \theta, \phi) \\ &\quad \xi/[\alpha(t-f) - \xi]|_{f=0} \\ &\quad + \alpha/2[1 + z^2/(\alpha(t-f) - x)^2] M'(\xi(f), \theta, \phi) \\ &\quad \times \alpha(\xi - \alpha/2(t-f)[1 + z^2/(\alpha(t-f) - x)^2] \\ &\quad /(\alpha(t-f) - \xi)^2|_{f=0} \\ &= \alpha^2 z^2/(\alpha t - x)^3 M'(\xi, \theta, \phi)\xi/(\alpha t - \xi) \\ &\quad + \alpha/2[1 + z^2/(\alpha t - x)^2]\partial_\xi M'(\xi, \theta, \phi)\xi/(\alpha t - \xi) \\ &\quad + \alpha^2/2[1 + z^2/(\alpha t - x)^2] M'(\xi, \theta, \phi) \\ &\quad \times \{\xi - \alpha t/2[1 + z^2/(\alpha t - x)^2]\}/(\alpha t - \xi)^2 \end{aligned}$$

for time $t = \{\xi + [(\xi - x)^2 + z^2]^{1/2}\}/\alpha$ satisfying $\xi = (1/2)(\alpha^2 t^2 - r^2)/(\alpha t - x)$.

When x, $z \to 0$ only the middle term remains, $\alpha t \to 2\xi$, $\xi/(\alpha t - \xi) \to 1$, $\xi - \alpha t/2 \to 0$, and $I_1(t, \theta, \phi) \to \alpha/2 \partial_\xi M'(\xi, \theta, \phi)$ as derived in the main text. When $r \gg \xi$, $r \to \alpha t$, $\xi/(\alpha t - \xi) \to \xi/r$, $\alpha^2 z^2/(\alpha t - x)^3 \sim O(1/r)$, $\alpha/2\ [1 + z^2/(\alpha t - x)^2] \sim O(1)$, $\{\xi - \alpha t/2[1 + z^2/(\alpha t - x)^2]\}/(\alpha t - \xi)^2 \sim O(1/r)$, and $I_1(\theta, \phi)$ reduces to two terms $\sim O(1/r)$ with coefficients $\approx \xi \partial_\xi M'(\xi, \theta, \phi)$ and $\approx M'(\xi, \theta, \phi)$.